ACS MATERIALS Au
AN OPEN ACCESS JOURNAL OF THE AMERICAN CHEMICAL SOCIETY

pubs.acs.org/materialsau
Article

Resistive Avalanches in $La_{1-x}Sr_xCoO_{3-\delta}$ (x = 0, 0.3) Thin Films and Their Reversible Evolution by Tuning Lattice Oxygen Vacancies (δ)

Published as part of ACS Materials Au virtual special issue "2023 Rising Stars".

Soumya Biswas, Noora Naushad, Kalyani S, and Vinayak B. Kamble*

Cite This: ACS Mater. Au 2024, 4, 308−323
Read Online

ACCESS | Metrics & More | Article Recommendations | Supporting Information

ABSTRACT: Strong correlations are often manifested by exotic electronic phases and phase transitions. $LaCoO_{3-\delta}$ (LCO) is a system that exhibits such strong electronic correlations with lattice−spin−charge−orbital degrees of freedom. Here, we show that mesoscopic oxygen-deficient LCO films show resistive avalanches of about 2 orders of magnitude due to the metal−insulator transition (MIT) of the film at about 372 K for the 25 W RF power-deposited LCO film on the Si/SiO_2 substrate. In bulk, this transition is otherwise gradual and occurs over a very large temperature range. In thin films of LCO, the oxygen deficiency ($0 < \delta < 0.5$) is more easily reversibly tuned, resulting in avalanches. The avalanches disappear after vacuum annealing, and the films behave like normal insulators (δ ~0.5) with Co^{2+} in charge ordering alternatively with Co^{3+}. This oxidation state change induces spin state crossovers that result in a spin blockade in the insulating phase, while the conductivity arises from hole hopping among the allowed cobalt Co^{4+} ion spin states at high temperature. The chemical pressure (strain) of 30% Sr^{2+} doping at the La^{3+} site results in reduction in the avalanche magnitude as well as their retention in subsequent heating cycles. The charge nonstoichiometry arising due to Sr^{2+} doping is found to contribute toward hole doping (i.e., Co^{3+} oxidation to Co^{4+}) and thereby the retention of the hole percolation pathway. This is also manifested in energies of crossover from the 3D variable range hopping (VRH) type transport observed in the temperature range of 300−425 K, while small polaron hopping (SPH) is observed in the temperature range of 600−725 K for LCO. On the other hand, Sr-doped LCO does not show any crossover and only the VRH type of transport. The strain due to Sr^{2+} doping refrains the lattice from complete conversion of δ going to 0.5, retaining the avalanches.

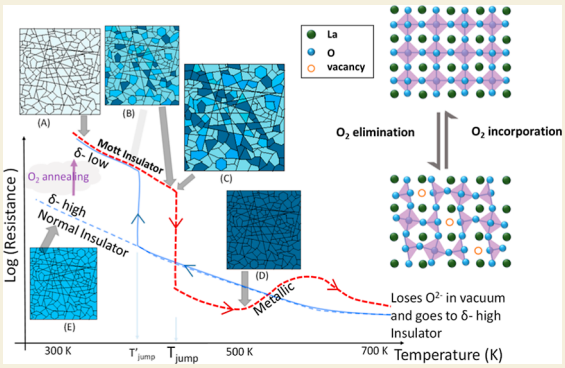

KEYWORDS: *lanthanum cobaltate, oxygen vacancies, resistivity, avalanches, metal35 insulator transition, hopping*

1. INTRODUCTION

Phase transitions of conventional to exotic phases of matter have been an intriguing subject of study in condensed matter sciences. The order parameters driving such phase transitions manifest differently across many experimental systems. Assorted instances comprise the magnetocaloric effect in several alloys,[1] Barkhausen noise in magnetic materials[2,3] acoustic emission in martensitic transition,[4,5] structural phase changes in materials,[6,7] etc. The abrupt step-like resistance changes have been known in several systems, including Mott transitions involving strong electron correlation effects.[8−10] Once the system transforms into the stable (crystalline) phase under heat treatments with the given thermodynamic conditions, it seldom traces back the same path during cooling.[11] For instance, in amorphous $Ge_2Sb_2Te_5$, the memory phenomenon was reported by Ozatay et al.[12] and Cheng et al.[13] to be mainly the electric field-induced crystallization of the films. Here, the driving force of the crystallization is reported to be the applied potential, where a threshold voltage triggers the phase transition. The reset condition is achieved when a pulsed laser is used to cause local heating, followed by melt quenching for amorphization. VO_2 is another Mott insulator that shows a hysteretic phase transition from the insulating to metallic state just above room temperature and is of enormous interest for optoelectronics.[14] Genchi et al.[15] reported a step-like resistance change, whereas Sharoni et al.[16] showed the steps occurring in multiples for VO_2 thin films in the vicinity of the metal to insulator phase Transition (MIT). Moreover, the abrupt jumps in resistance strongly abide by the power law as the device dimensions are scaled down. Nevertheless, such resistive avalanches could not be seen in

Received: November 23, 2023
Revised: January 18, 2024
Accepted: January 23, 2024
Published: February 2, 2024

complex and strongly correlated transition metal oxides, to the best our knowledge, which exhibit a plethora of magneto-electronic phases and phenomena.[17]

Recently, $LaCoO_{3-\delta}$ (LCO) has attracted renewed interest due to the observation of unconventional strain-induced ferromagnetism in thin films.[18−20] The bulk $LaCoO_3$ is nonmagnetic at low temperatures, with Co^{3+} ions having a low spin (LS) configuration (S = 0). However, the LCO epitaxial thin films with a small lattice mismatch grown on various substrates exhibit a ferromagnetic ground state with an unambiguous T_C of 85 K. Besides, Sr doping at the La site results in excess hole doping, which also introduces a strain in the $La_{1-x}Sr_xCoO_3$ lattice, bringing about Co^{4+} ions for charge compensation. This modifies the nature of the exchange coupling, converting the super exchange (SE) among Co^{3+} ions in LCO to double exchange (DE)[21] between Co^{3+} and Co^{4+} ions. Moreover, the presence of Sr leads to La site disorder. The resulting inhomogeneous lattice distortions amend the crystal field splitting and, consequently, the spin state of Co ions. Oxygen stoichiometry plays a crucial role in determining the physical properties and potential application of transition metal oxides (TMOs). A small change in the lattice oxygen content can result in a considerable variation of the oxidation state of the transition metal, drastically modifying the functionalities of the oxides.

According to the literature,[22] if the pristine $LaCoO_3$ lattice is considered, then the maximum number of oxygens that could be lost without affecting the parent crystal structure is less than one in every six lattice oxygens (two formula units) of pristine $LaCoO_3$. Losing 1 oxygen complete per two formula units distorts the structure and leads to the formation of another well-known structure called Brownmillerite (BM) LCO with the formula $LaCoO_{2.5}$, as shown in Figure 1b

$$2LaCoO_3 \xrightarrow{-\frac{1}{2}O_2} La_2Co_2O_5 \rightarrow 2LaCoO_{2.5} \quad (1)$$

Therefore, here, 1/6 defines the fraction of the total number of oxygen atoms present in the pristine $LaCoO_3$ lattice and not of x. With several synthesis processes, an oxygen-deficient stable structure of BM LCO2.5 ($LaCoO_{2.5}$) could be prepared.

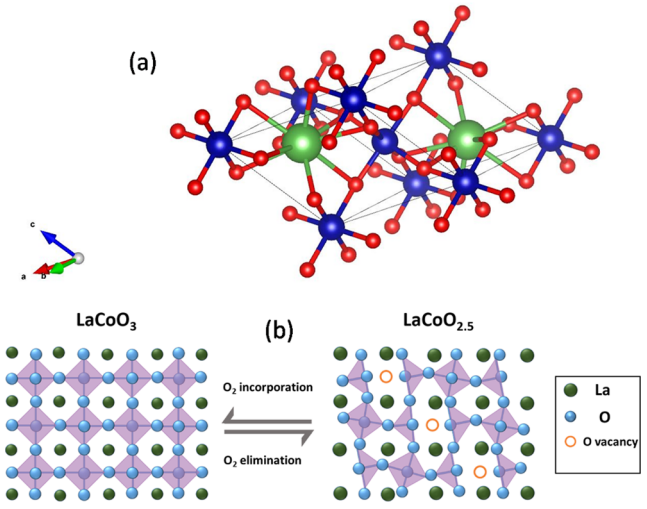

Figure 1. (a) Crystal structure of $LaCoO_3$. Green Co, blue La, and red O. (b) Structures of perovskite $LaCoO_3$ and BM $LaCoO_{2.5}$ and reversible O_2 incorporation—elimination into the $LaCoO_3$ lattice.

In this case, oxygen ion vacancies order at every alternate octahedron, resulting in the breaking of the octahedral structure and forming alternate square pyramids, as reported by An et al.[22] (see Figure 1b). $LaCoO_3$ may also exist in the oxygen-deficient stoichiometry of $LaCoO_{3-\delta}$, where $0 < \delta < 0.5$ (see Figure 1). Hitherto, in the $LaCoO_3$ and $La_{0.7}Sr_{0.3}CoO_3$ films, the MIT is a well-observed phenomenon.[23−25] The studies reported so far[26] state that in $LaCoO_3$, the ground state consists of only Co^{3+} ions specifically in the $3d^6$ spin configuration. At low temperatures (below 50 K), it remains in the LS state, i.e., S = 0 ($t_{2g}^6e_g^0$). In this case, the crystal field energy is comparable to the Hund's energy at high temperature (40 K < T < 150 K), i.e., LS Co^{3+} ions convert to the high spin (HS) state Co^{3+} ($t_{2g}^4e_g^2$) ions due to local excitation.[26] In the temperature range of 150−300 K, the numbers of Co^{3+} ions present in the LS and HS states are comparable. At T > 500 K, Co^{3+} disproportionates into Co^{2+} and Co $^{4+}$ due to the reaction between two consecutive Co^{3+} ions.

Upon doping with Sr^{2+} ions at the La^{3+} site in LCO, the number of Co^{4+} ions is increased to balance the charge. This leads to a hole doping in the system. In thin films having an inhomogeneous distribution of Co^{4+} ions, this doping creates a hole-rich region and a hole-poor region within the same $La_{1-x}Sr_xCoO_3$ film. This is generally dependent on the synthesis or the growth conditions of the films. However, the jump in the resistance with the increase in temperature has not been widely reported. In this paper, to the best of our knowledge, we report the first observation of single and multiple step-like resistance changes in the $LaCoO_3$ and $La_{0.7}Sr_{0.3}CoO_3$ films, albeit with a much lower transition temperature. With repeated measurement cycles, the films lose the behavior of the step jump in resistance. However, the behavior was partially re-established by the oxygen annealing, which can be portrayed as the reset button in the point of view of the memory device.

2. EXPERIMENTAL SECTION

2.1. Bulk Preparation

The undoped and Sr-doped $LaCoO_3$ samples were prepared by solid-state synthesis. After the dehydration step of hygroscopic La_2O_3, stoichiometric amounts of La_2O_3, $SrCO_3$, and Co_3O_4 were mixed and ground in a motor and pestle. In the case of $LaCoO_3$, the precursors used were La_2O_3 and $Co(NO_3)_2{\cdot}6H_2O$. The mixture was calcined at the rate of 3 °C/min at 1100 °C for 20 h. The heated mixtures of doped and undoped $LaCoO_3$ were hydraulic pressed into two separate pellets of 25 mm, which were then calcined at 1100 °C for 12 h at the rate of 5 °C/min. The pellets were subjected to X-ray diffraction (XRD) to assess their purity and phase formation.

2.2. Thin Film Deposition

The commercial Si/SiO_2 substrates were cut and cleaned with isopropyl alcohol followed by a soap solution and deionized water. The deposition parameters are described in Table S1 in the Supporting Information. In order to measure thickness, some of the film substrates were partially covered during the deposition. The film thicknesses measured for films at a given RF power and time of depositions have been shown with a gradient plot in Figure S1 in the Supporting Information. Films deposited at 25 and 50 W RF powers are hereafter referred to as LCO_25 and LCO_50, respectively. Similarly, Sr-doped films deposited at 25 and 50 W RF power are referred as LSCO_25 and LSCO_50, respectively. The 25 W, 1 h deposited films of $LaCoO_3$ (LCO_25) as well as of $La_{0.7}Sr_{0.3}CoO_3$ (LSCO_25) are about 125 nm in thickness (see the Supporting Information for target XRD data in Figure S2 as well as thin film deposition parameters).

https://doi.org/10.1021/acsmaterialsau.3c00101
ACS Mater. Au 2024, 4, 308−323

2.3. Characterization and Measurements

The as-prepared and sintered films were examined using a Bruker X-ray diffractometer having a Cu K_α X-ray source of 0.15418 nm in the range of 10−60° and a step size of 0.017°. X-ray photoelectron spectroscopy (XPS) measurements were carried out using an Omicron X-ray photoelectron spectrometer with a Mg source (1253.6 eV). The resistance measurement was carried out by the 4-probe van der Pauw method using. The thickness of the films was measured by the profilometer KLA-TENCOR D-600. The elemental composition and oxidation states of the films were evaluated using XPS, which allows the measurement of the binding energy with high resolution. A Mg K_α incident photon energy of 1253.6 eV was used to evaluate the composition. C 1s with a binding energy of 284.6 eV was used as the reference for binding energy corrections. The binding energies reported here have an accuracy of ±0.3 eV.

The measurement was taken by the Keithley 2700 multimeter cum data acquisition system. This is programed in such a way that it can apply the full range of current and measure the voltage to give the final resistance value in a four probe fashion. When it is unable to pass the full range of current, automatically, a lower value of the current is sent. If the voltage drop is more than the compliance value due to the given current, it adjusts self-consistently and takes the proper readings. The range of accurate resistance measurement is 100 Ω to 100 MΩ. Besides, in this point, it is crucial that the $I-V$ characteristics should be linear and should pass near the origin (i.e., no offset). The $I-V$ characteristics were measured in the high resistive as well as the low resistive state, and the same are presented for LCO_25 and LSCO_25 (see Figure S5 in the Supporting Information).

Before every deposition, the commercial Si/SiO_2 substrate was preannealed for the formation of a complete layer of SiO_2. The $I-V$ curve of the SiO_2 substrate is obtained at room temperature (300 K) as well as at 523 K. This SiO_2 layer is highly resistive, which has a negligible effect as the leakage current. The $I-V$ curve of the SiO_2 substrate is presented in Figure S5 in the Supporting Information. Besides, the nature of the resistivity graphs specially in the heating cycle is mainly due to the LCO samples. Otherwise, with the contribution from SiO_2, the trend would not have been the same.

3. RESULTS AND DISCUSSION

3.1. Structural Analysis Using X-Ray Diffraction

The crystal structure of pristine $LaCoO_3$ is shown in Figure 1a, which clearly defines the perovskite form of the material.[27] The evolution of the crystal structure of the BM phase ($LaCoO_{2.5}$) from the perovskite phase ($LaCoO_3$) and vice versa due to the removal and incorporation of O_2, respectively, are shown in Figure 1b. To investigate the phase formation and its evolution, XRD measurements were performed on as-deposited films as well as after each subsequent annealing treatment (in vacuum as well as in oxygen). The obtained XRD patterns are shown in Figure 2. Because of the low thickness of the thin films, it may be seen that the substrate peaks are very prominent and have higher intensities than that of the film reflections. For comparison, the XRD pattern of the bare $Si-SiO_2$ substrate is also shown in Figure 2a(iv). It could also be inferred that the as-deposited LCO and LSCO films' X-ray patterns are amorphous in nature, as seen in Figure 2a(i),c(i), where both show a broad glass-like hump at 40°.

The XRD pattern is recorded after vacuum annealing and 100% oxygen annealing for the LCO_25 film at 500 °C, as shown in Figure 2a(ii,iii). The XRD pattern of the LSCO_25 film annealed at 500 °C in vacuum is shown in Figure 2c(ii). It is seen that the XRD peaks of both the films appear after annealing in vacuum [Figure 2a(ii),c(ii)] as well as in oxygen at 500 °C [Figure 2a(iii)]. This marks the improved crystallinity of the samples as these are heated in vacuum. Similar treatment and measurements were performed on the

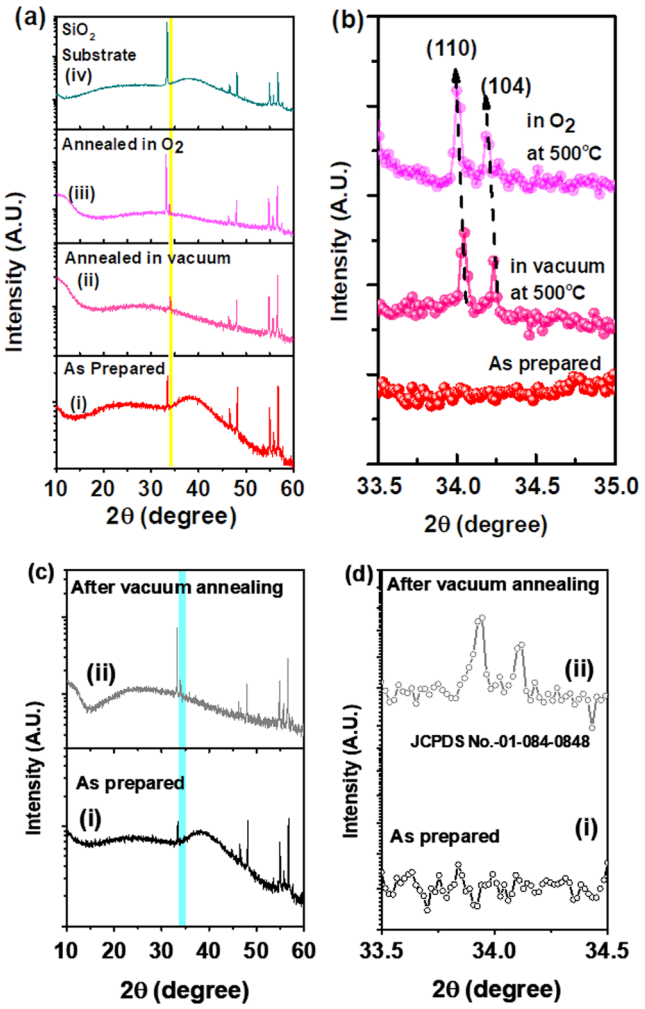

Figure 2. XRD patterns of (a) LCO_25 and (c) LSCO_25 thin films for as-deposited (i), vacuum-annealed (ii), and oxygen-annealed (iii) thin films. (b,d) show the magnified view of the (110) and (104) peak evolution as a result of annealing. For comparison, bare Si/SiO_2 substrate data are also shown in (a) (iv).

LCO_50 (deposited at an RF power of 50 W for 1 h) and LSCO_50 films, and the XRD patterns are reported in Figure S3a,c, respectively. Expecting further enhancement in crystallinity, the LCO_50 film was heated to 900 °C in an oxygen-rich environment. The XRD pattern of this film is shown in Figure S4.

Figure 2b shows the enlarged view of the XRD peaks of the LCO_25 film. It may be observed that when this film is annealed in vacuum at 500 °C, the crystallinity of the LCO increases, resulting in the appearance of the two peaks of (110) and (104).[28] This matches with the peaks of the $LaCoO_3$ polycrystalline powder as given in Figure S2 with the JCPDS no. 01-084-0848.[29] Further, on annealing it in an oxygen-rich atmosphere at 500 °C, not only does the peak intensity decrease but there is also a slight shift toward a low Bragg angle. The enlarged view of the XRD pattern of the LCO_50 film is shown in Figure S3b. To observe the further effect of oxygen in the crystallinity, the LCO_25 film is annealed at high temperature in oxygen, and XRD is performed (see Figure S4). On annealing the film at an even higher temperature (900 °C), there is a higher shift, and the intensity further decreases (see Figure S3b). The Bragg angle of the (110) peak was

https://doi.org/10.1021/acsmaterialsau.3c00101
ACS Mater. Au 2024, 4, 308−323

observed to decrease consistently from 33.82° for the film annealed at 500 °C to 33.78° for the film annealed at 900 °C in an oxygen-rich atmosphere. The shift in the XRD peaks is likely to be a consequence of the change (increase) in the average lattice spacing due to oxygen incorporation, which is a result of the relaxation of residual stresses occurring due to oxygen vacancies in the as-prepared films. The magnified view of LSCO_25 and LSCO_50 films were shown in Figures 2d and S3d). It also shows the (110) and (104) peaks similar to the LCO films. However, these peaks were found at a lower Bragg angle of 33.9 and 34.1°, respectively. Sr^{2+} being larger than La^{3+}, the shift in Bragg angles confirm the Sr doping in the LCO lattice. The same is confirmed via the chemical composition, and the charge states of elements are probed via XPS on the LSCO_25 film, as presented in the subsequent sections.

In order to rule out the possibility of the measurement artifact, the following argument may be considered. The film is deposited on the Si substrate having naturally grown a SiO_2 layer, and LCO films are deposited subsequently. When such a film is subjected to the XRD, irrespective of the thickness of the film, the XRD peak of the Si substrate should appear at the same 2θ value. Every pattern is calibrated with respect to this Si peak. Moreover, the similar nature of the change in the peak position toward a low Bragg angle (toward the Si peak) after annealing in all the samples irrespective of the doped or undoped composition and similar thickness diminishes the scope of the measurement artifact, in which case it would be completely random. As mentioned in the Experimental Section, the step size used for XRD measurement is 0.017°, which is 1 order of magnitude lower than the difference in the peak position observed, for instance, 34.32 − 34.20 = 0.12°. Therefore, the peak position shift cannot be ruled out as an experimental artifact.

The bulk XRD data shown in Figure S2 in the Supporting Information are used as a reference for comparing the XRD patterns of the films. It may be noted from Figure S2 that the two most intense peaks are for (110) and (104) reflections. The other peaks have a 50% or lower intensity than these two. Besides, this also implies that these two planes are the maximally dense planes, with densely packed scatters (atoms).[7,30,31] Therefore, when the film is grown on an amorphous substrate like SiO_2, due to the lack of any epitaxy and the lack of crystallization energy (no heater used during deposition), the as-prepared film is amorphous in nature.

When the film is annealed for the first time, the thermal energy induces crystallization, and the system nucleates in its least formation energy planes, which are the most densely packed crystal planes. However, multiple nucleation sites may lead to multiple crystallites within the film having the same out of-plane orientation but all possible in-plane orientations called texture.[32] Therefore, when X-rays are incident on such a film, the diffraction pattern mostly contains only a few peaks pertaining to the crystalline orientation fraction. It is important to note that thin film texture differs from that of the epitaxy, where there is a single orientation throughout the film that is governed by crystal matching with the substrate, whereas texture may have a partial or preferred orientation.[31] An example of texture can be found in Figure 3 of ref 31 as a valuable resource for the reader where fractional orientation patterns are shown for the same crystal structure. Therefore, we believe that the other planes may not be significantly oriented in order to contribute toward the diffraction.

3.2. Electric Transport Studies

The four-probe resistance of the as-deposited LCO and LSCO films were measured as a function of temperature under vacuum ($\sim 10^{-2}$ mbar). Each measurement comprised data recorded during heating and cooling cycles. Subsequent trials of resistance measurement were carried out sequentially. This was followed by annealing the films at 500 °C for 2.5 h in vacuum and cooling them down naturally. For most of the films, it is evident that the first trial of the as-deposited film showed a significant variation in resistance compared to the subsequent ones. The measurements of films in different atmospheric conditions are tabulated in Table S1 in the Supporting Information.

Figure 3a shows the measurement of pristine LCO_25 samples, while Figure 3d show the same for LSCO samples. As

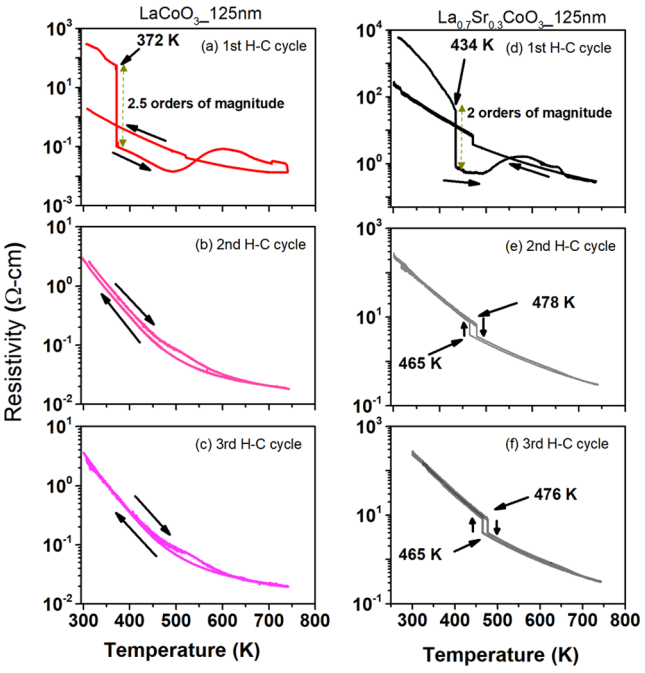

Figure 3. Resistance as a function of temperature of subsequent trials for films of 125 nm thickness: (a−c) LCO_25 and (d−f) LSCO_25 films deposited on a Si−SiO_2 substrate.

seen in the figure, the LCO_25 film showed a prominent hysteresis in heating and cooling data vis-à-vis sudden jumps corresponding to the MIT in the range of 350−600 K, characterized by a change of slope of R vs T.[33] The sudden jump in resistance is of 2 or more orders of magnitude. This is in good accordance with the temperature values reported in the literature.[33,34] The first (virgin) trial of all the LCO_25 and LCO_50 samples exhibits a very prominent jump that diminished in the subsequent trials, wherein they behave like a normal insulator.[33] Interestingly, a broad peak is observed in the virgin heating curves from 550 to 650 K. Here, the virgin curve shows a large variation in resistance with the existence of the same peak at 550 to 650 K, followed by a decrease during cooling. Figure 3b depicts the subsequent (2nd) trial of measurement performed in vacuum of LCO_25. Similarly, Figure 3c shows the third trial of the same samples measured under the same condition. The similar experiments were performed on the LCO_50 film to check the dissimilarities with respect to the deposition power. However, an almost

https://doi.org/10.1021/acsmaterialsau.3c00101
ACS Mater. Au 2024, 4, 308−323

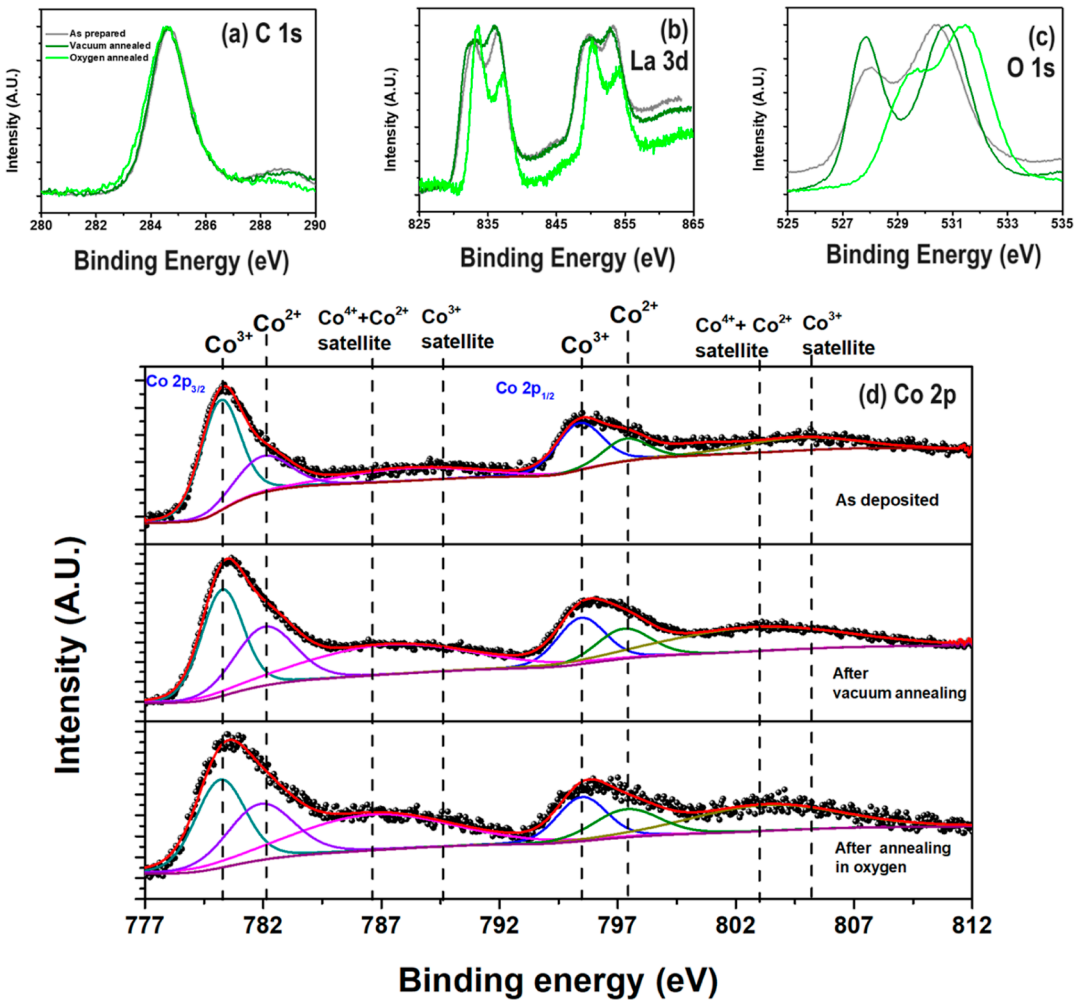

Figure 4. X-ray photoelectron spectral comparison of as-prepared, vacuum-annealed, and oxygen-annealed LCO_25 thin films for (a) C 1s, (b) La 3d, (c) O 1s, and (d) Co 2p core levels.

similar outcome compared to the LCO_25 film is observed as shown in Figure S6a−c. In the case of LCO_25, a faster loss of the avalanche step jump is observed with the consecutive trials.

The drastic changes during the first heating cycle data of the film may be attributed to the in situ crystallization of the films as well as the dynamic reorganization of the spins within the crystallite. A crystallite refers to small domains having only one crystal orientation. The film may be composed of a large number of crystallites arranged in the same or different directions. If they are oriented preferentially along the same direction, the film is said to textured and it shows one single peak (and its higher order peaks) in the XRD pattern. The XRD pattern in this case revealed sharp peaks just after the first trial of heating. As discussed earlier, the loss of the lattice O^{2-} ions is anticipated during the measurements due to the in situ annealing happening in vacuum. This significant loss of oxygen from $LaCoO_3$ could lead to the metastable oxygen-deficient structural phases (BM $LaCoO_{2.5}$ and $LaCoO_{2.67}$), as shown in Figure 1b.[34] Such a phase transformation could lead to the observed change with the subsequent trials as the solid loses more and more oxygen.

As reported by An et al.,[22] for a stabilized oxygen-deficient $LaCoO_{3-\delta}$, the maximum oxygen vacancy that the structure can hold is 1/6th of the total lattice oxygen of pristine $LaCoO_3$. This is probably the reason that after the second trial, no further change was observed in the $R-T$ data except the diminishing of the hump near the transition. It is well established that the hysteresis observed during the heating and cooling occurs due to the underlying first order nature of the Mott transition in LCO.[35,36] As the samples go through a controlled heating and a natural cooling, along with the continuous removal of oxygen (δ starts to increase to reach near the value 0.5), hysteresis is generated.

3.3. Nonstoichiometry and Origin of the Metal Insulator Transition in LCO

The XPS measurements are done on the LCO_25 films deposited for 1 h in order to study the composition and stoichiometry. C ls, La 3d, and O ls core levels were recorded and are shown in Figure 4. All binding energies reported were referenced to the C ls photoemission at 284.6 eV to correct the charge shift (Figure 4a), if any. The La 3d shows two peaks as displayed in Figure 4b due to spin−orbit interactions ($3d_{5/2}$ and $3d_{3/2}$). Besides, each peak is also doubly degenerate, which denotes a satellite from $3d^04f^1$ other than the expected $3d^04f^0$. Ichimura et al.[37,38] reported the presence of two kinds of oxygen species in $LaCoO_3$ by XPS. In Figure 4c, in the O 1s spectra, two well-defined photoemission lines at binding energies of 528.2 and 531.3 eV are observed. The first of these lines is assigned to lattice oxygen.[39,40] The second line is assigned to adsorbed oxygen (O^-) or OH^-. The line at 531.3

https://doi.org/10.1021/acsmaterialsau.3c00101
ACS Mater. Au 2024, 4, 308−323

eV is broader than the line at 528.2 eV. This suggests that adsorbed oxygen or hydroxyl groups exist in a rather wide distribution of states. Their relative ratio shows that the as-deposited film has more surface adsorbed oxygen than the lattice oxygen contribution. It reduces to almost 1:1 in vacuum-annealed films, and upon oxygen annealing, it again becomes almost similar to the as-deposited film. We tried to quantify the stoichiometry from the XPS data. The formulas of the films are as shown in Table 1.

Table 1. Compositions Calculated from XPS Data

LCO_25 film stages	film nominal composition
LCO as-deposited	$LaCo_{0.971}O_{3.49}$
LCO after 2nd vacuum annealing	$LaCo_{0.967}O_{2.77}$
LCO after oxygen annealing	$LaCo_{0.967}O_{2.97}$

The quantification reveals that the least oxygen is present in the twice vacuum-annealed film, which supports our conjecture. However, the quantity is only indicative as the XPS is a surface (top 5 nm) sensitive technique. In the as-deposited film, the crystallization is coupled along with the oxygen mobility in/out from the lattice; therefore, the oxygen-annealed film showed relatively less oxygen than the as-deposited film. Hence, a large jump (~2.5 orders of magnitude) is observed in as-deposited LCO along with an excessive loss of oxygen. Thus, a clear correlation can be seen in the oxygen content of the lattice and the magnitude of the sudden jump in resistivity by this nominal quantification.

The spectrum of Co 2p in $LaCoO_3$, (Figure 4d) exhibits a multiplet splitting of about 15.3 eV [with (Co ($2p_{3/2}$) at 780.2 eV and Co ($2p_{1/2}$) at 795.5 eV)] for Co^{3+} ions. For further investigation and quantification of Co ions, the Co 2p spectra are deconvoluted for all the three samples. As mentioned by Wang et al.,[39] in the Co $2p_{3/2}$ spectrum, a peak was observed at the binding energy of 780.3 eV due to the Co^{3+} in the octahedral coordination, and another peak was observed at 782.1 eV corresponding to Co^{2+} in the tetrahedral coordination in all the three XPS spectra. Formation of Co^{2+} upon reduction of the starting perovskite can be detected by the appearance of two shakeup satellite peaks,[20] which are situated at about 6.5 and 9.7 eV upscale from the peaks for Co^{3+} due to the presence of Co^{2+} along with Co^{4+} and Co^{3+} ions, respectively. These satellites can be considered as the fingerprints of these ions since the spectral lines of the multiplets for both Co^{3+} and Co^{2+} are practically coincident.[41] It is noted that these satellite peaks are indeed present in the spectrum of $LaCoO_3$ (Figure 4d). Based on these spectra, the ratio Co^{2+}/Co^{3+} is calculated for the films, and further discussion is presented in the latter part of this paper.

In Figure 4, even though there is no change in the binding energy of the C 1s reference peak, all the peaks in the three samples show a systematic change with annealing. Compared to those of the as-prepared sample, the spectra of the vacuum-annealed sample are shifted to lower binding energy and the spectra of oxygen-annealed samples are shifted to higher binding energy. The change in binding energies marks the change in Fermi levels of the three compositions due to the change in defect-induced carrier concentrations.

To confirm the presence of Sr in the LSCO films, XPS was also performed on a LSCO_25 film. Figure 5a–c shows the comparison of La 3d, Sr 3d, and O 1s peaks of LSCO and LCO thin films, respectively. In Figure 5d, the Co 2p peak of the same sample is shown along with the Co 2p peaks of the LCO_25 sample for comparison. The Sr inclusion in the LCO lattice site gives rise to the Co^{4+} satellite peak.

As seen in Figure 5, on Sr^{2+} substitution at the La^{3+} site, excessive positive charge deficiency is created within the lattice, and this induces Co^{3+} to Co^{4+} oxidation to maintain charge neutrality of the crystal. This leads to high hole doping in the system, and therefore, the excess carriers change the chemical potential. The change in the Fermi level (zero binding energy) position is seen as a shift in the core level peaks. This also agrees with the increase in the relative fraction of Co^{4+} in LSCO in comparison to that in LCO, as is seen in Figure 5d. It confirms that the Sr doping at the La site is compensated by

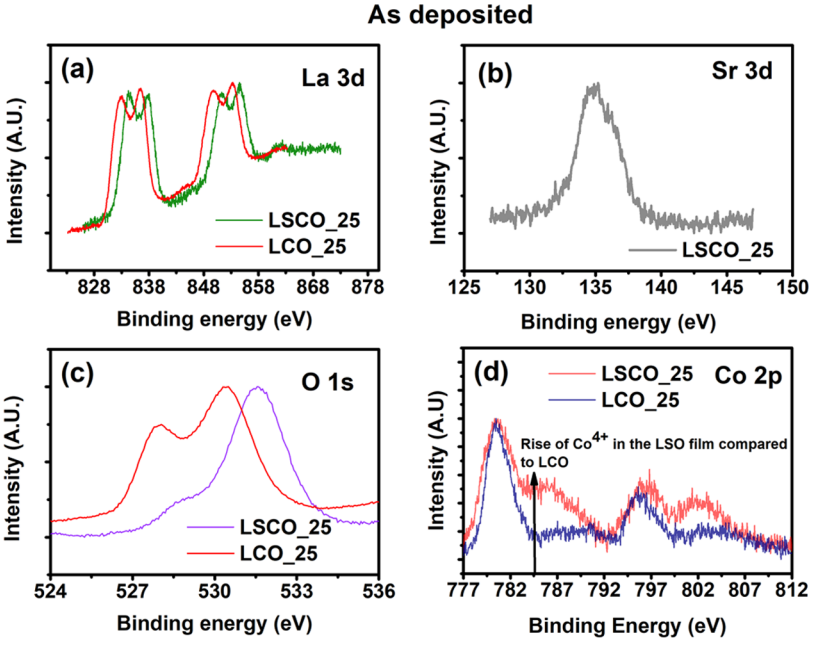

Figure 5. Comparison of the XPS spectra of (a) La 3d, (b) Sr 3d, (c) O 1s, and (d) Co 2p of the LSCO_25 and LCO_25 as-deposited films.

https://doi.org/10.1021/acsmaterialsau.3c00101
ACS Mater. Au 2024, 4, 308–323

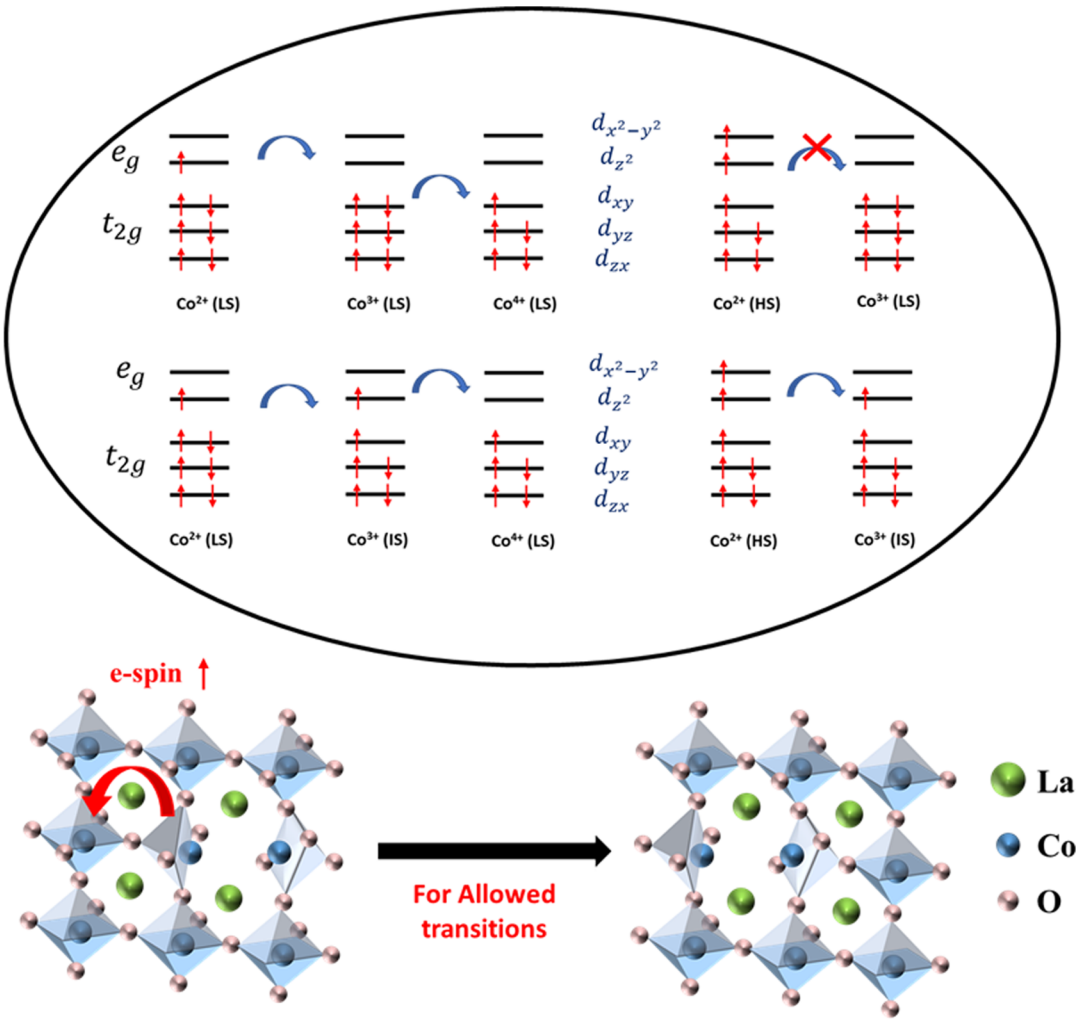

Figure 6. Spin state transition through the double exchange electron hopping mechanism in the insulating phase.

the increase in Co ion stoichiometry from Co^{3+} to Co^{4+}. The excess number of Co^{4+} ions stabilize the lattice relative to the LCO lattice.

This nonstoichiometry in Co as well as corresponding oxygen ions is primarily responsible for the rich transport properties of the system. There are several reports that explain the MIT phenomenon of the $LaCoO_3$ films with the help of the charge- and spin-dependent transport.[24−26] As mentioned earlier, the conduction mechanism in this type of transition metal oxides having a perovskite structure primarily is due to the spin state transition. (Other than cobaltate, it is found in nickelate, cuprate, manganites, etc.)[42] At low temperature, in the insulating phase, the Co^{3+} ions mainly exist in the LS state ($S = 0$, i.e., $t_{2g}^6\ e_g^0$) configuration of CoO_6 octahedra. At temperatures $T < 100$ K, 50% Co^{3+} exist in the LS state and the rest of Co^{3+} exist in the HS state ($S = 2$, i.e., $t_{2g}^4\ e_g^2$). In the temperature range of 100 K $< T <$ 350 K, the number of Co^{3+} ions in the HS state remains unchanged, while the Co^{3+} in the LS state start converting to Co^{3+} intermediate spin (IS) states ($S = 1$, i.e., $t_{2g}^5\ e_g^1$). Further, for 350 K $< T <$ 650 K, an insulator to metal transition occurs, where the current study is pertinent. In the semiconducting ($T < T_{MIT}$) phase, there is a coexistence of Co^{3+} in the LS, IS, and HS state. However, in the metallic phase ($T > T_{MIT}$), almost all the LS Co^{3+} transform into IS Co^{3+}. Thus, the resistive transition is brought about by these 50% Co^{3+} in the IS state and 50% Co^{3+} in the HS state that exist in the metallic phase (the tail of the hump observed in $R-T$).

Previous reports suggest that above 200 K, Co^{3+} ions have the possibility to undergo the disproportion reaction as well, which creates Co^{2+} and Co^{4+} ions. In the oxygen-deficient samples, Co^{2+} ions exist in the square pyramid coordination (where one of the six oxygen ions of the octahedron is missing). Hence, below the T_{MIT}, the transport occurs only via the "allowed" hopping of a hole from Co^{3+} ions to the LS states Co^{4+} ions. However, the electron hopping from the HS Co^{2+} ions to LS Co^{3+} ions is forbidden because of the spin blockade, as shown schematically in the Figure 6 upper panel.[43] Consequently, the electrons are localized on HS state Co^{2+} ions. However, around the T_{MIT} range or higher, the Co^{3+} ions exist in the mixed spin states. This allows both the electron and the hole to transport[26] by the hopping mechanism, and it improves the conductivity along with the MIT, as shown in the Figure 6 lower panel. Kumar et al. showed the reduction in the Seebeck coefficient in the aforementioned temperature range in their studies for $La_{1-x}Sr_xCoO_3$ samples.[44−46] In the present study, a similar MIT was observed in LCO films. However, during the cooling cycle, the resistivity seldom shows any sudden rise, and a normal insulator-type behavior is exhibited. When the films are held at high temperature for 2 h, the

https://doi.org/10.1021/acsmaterialsau.3c00101
ACS Mater. Au 2024, 4, 308−323

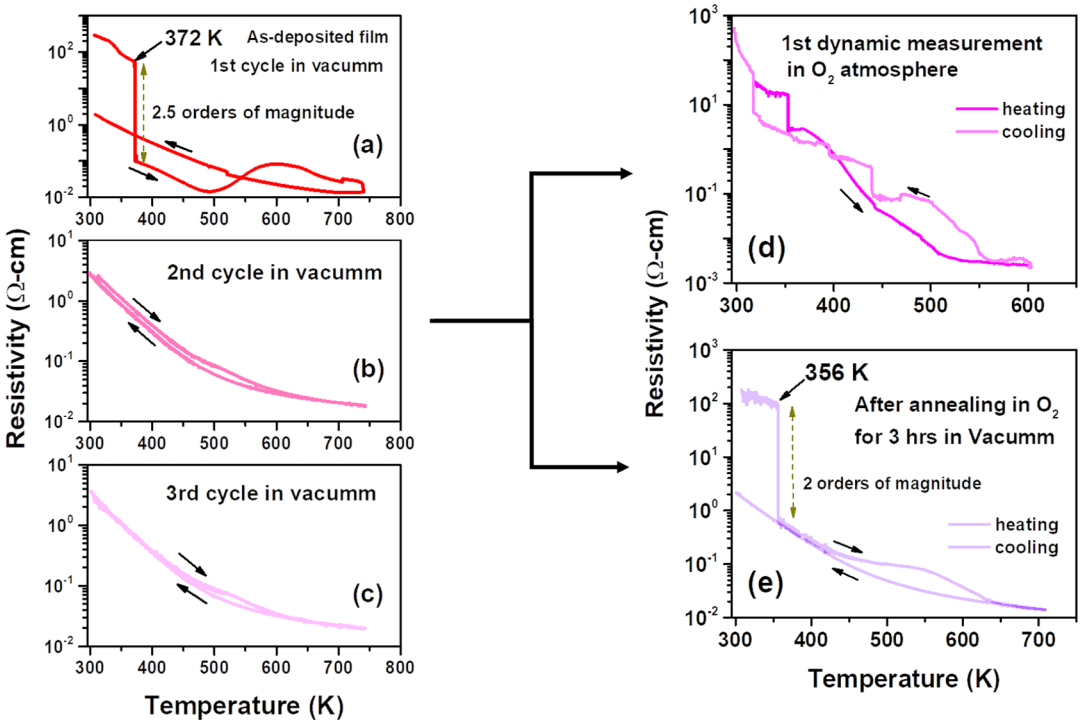

Figure 7. Resistance vs temperature plots for (a) as-prepared measured in vacuum, (b) 2nd trial measured in vacuum, (c) 3rd trial measured in vacuum, (d) measured in oxygen, and (e) oxygen-annealed LCO_25 films deposited for 1 h on the Si−SiO_2 substrate.

annealing of films takes place at high temperature as mentioned, leading to the loss of oxygen from the lattice sites. This loss of oxygen breaks two consecutive octahedra, generating square pyramids (as shown in the Figure 6 lower panel), thereby introducing more Co^{2+} ions.[34] As increasing number of oxygen vacancies are formed in the lattice sites, leading to conversion of square pyramids into tetrahedra as well as their ordering alternate layers. As a result, the electronic states developed from oxygen-deficient Co ions (CoO_4 tetrahedra and CoO_5 pyramids) as well as from the adjacent octahedral Co ions become more localized, and the film exhibits a normal insulating behavior throughout the cooling cycle, as observed in Figure 3a. It is important to note that during the next heating cycle, i.e., in Figure 3b, a further change in the slope is observed. This behavior may also be attributed to Co^{3+} ions. Although in the first cooling cycle, a typical insulating behavior is shown, there may be a few Co^{3+} IS ions reverting back to the LS state when the film is cooled down to room temperature. Besides, due to the continuous removal of oxygen, there may be generation of more reduced Co^{2+} ions. Consequently, in the next heating cycles, the change of the slope and the transition range of the temperature diminished gradually.

In order to study the effect of charge imbalance, it is probed via 30% Sr doping in LCO thin films. Unlike undoped LCO, Sr doping of 30% in the La sites stabilizes the Co^{3+} IS states in the pristine lattice of LSCO without the effect of temperature, unlike LCO films. From the previous reports, the LSCO films having 30% Sr were expected to follow a metallic character.[47,48] Nevertheless, the first trial of $R-T$ exhibited a behavior similar to that of the LCO films, as shown in Figure 3d. In the doped films, hole-rich and hole-poor regions may coexist. Hole-poor regions may act like an LCO film with the variation of temperature, while the hole-rich regions generate the Co^{4+} ions to compensate for the Sr^{2+} doping (see Figure 5). Due to the Sr^{2+} doping, the resistivity reduced and the lattice stabilized faster, reducing the probability of oxygen removal from the lattice right after the first trial of measurement. As a result, not much change was observed in the subsequent trials. In other words, the lattice is refrained from distortions for LSCO unlike that for LCO, in the temperature range of 300−650 K, as illustrated in Figure 3e,f for the second as well as third cycle of the $R-T$ measurement of LSCO_25, and similar results are also observed in the LSCO_50 films, as shown in Figure S5d−f. It depicts the consistency in the result.

3.4. Postoxygen Annealing vs Dynamic Oxygen Atmosphere Electrical Transport Measurements

In order to confirm the role of oxygen in the observed phenomena, an LCO thin film of about 125 nm thickness was annealed in the 100% oxygen atmosphere at 500 °C after two cycles in vacuum and the sample was subjected to the temperature-dependent resistance measurements. To investigate the in situ changes in the oxygen atmosphere, another film (already measured twice in vacuum) was measured in the presence of 100% oxygen. The comparisons are given in Figure 7d,e for $R-T$ measurement in an in situ oxygen atmosphere and post oxygen annealing vacuum measurement, respectively.

The film measured in the in situ oxygen atmosphere shows a continuous change in both the heating and cooling cycles, as displayed in Figure 7d. In the heating cycle, the MIT is well observed. Surprisingly, during the cooling, not only a big hump of MIT was observed but also a multistage resistivity change was detected, which is described in the following section. However, for the ex situ oxygen-annealed film measured in a vacuum atmosphere, it achieved a significant restoration of lattice oxygen, as is evident from the regeneration of the step-like transition seen in Figure 7e. Nevertheless, the phase transition could not be completely reversed, in the MIT transition range. Besides, the broad peak in $R-T$ around 500−

https://doi.org/10.1021/acsmaterialsau.3c00101
ACS Mater. Au 2024, 4, 308−323

600 K is also restored. It confirms the incorporation of the oxygen in the lattice sites throughout the measurement and subsequently the crystallite-wise metal to insulator conversion, which initiates the discontinuity in the percolation path and proclaims the multistep change in the resistivity. The mechanism is discussed in the following section.

With the expectation of further oxygen incorporation in the lattice site, the same film was heated at 900 °C for annealing for 150 min in the 100% oxygen atmosphere. This treatment may have caused a total surface reconstruction of the film, leading to randomness and an inhomogeneous nature such that the resistance became so high that it was arduous to perform a stable temperature-dependent resistance measurement. However, this needs to be further substantiated.

As reported by Okazaki and Tomiyasu, the resistivity in the $LaCoO_3$ films significantly reduces beyond T_{MIT}.[43] For the activation-type resistivity, it should follow the trend of resistivity as follows

$$\rho = \rho_a \exp\left(\frac{\Delta}{k_B T}\right) \tag{2}$$

where ρ_a and k_B are the extrapolation at high temperature and the Boltzmann constant, respectively. If the activation energy for the change in the resistivity is independent of temperature, $[\Delta/k_B T]$ will be equivalent to the first derivative of ln $\rho(T)$ with respect to $1/T$, i.e., $d(\ln(\rho))/d(T^{-1})$. The anomaly, in every $R-T$ measurement performed on the LCO_25 film, is clearly observed when the $d(\ln(\rho))/d(T^{-1})$ is plotted versus temperature.[43,49] The large peak indicates the steep metal−insulator crossover. Plateaus of the same curve observed at relatively low temperature correspond to the thermally activated conduction mechanism with a well-defined activation energy constant over a range.[50] The temperature at which the resistivity displays the point of inflections[51] is shown in Figure 8a, and the minimum is marked by the T_n*, while the maximum is marked by the $T_n^{\$}$ (n = 1, 2, 3, and 4) for the nth measurement cycle. For the vacuum measurement of the as-deposited film, i.e., n = 1 the temperature difference between the maximum and minimum is large. Moreover, during second cycle, the same is reduced and remains so for the third cycle. On the other hand, when the oxygen-annealed sample is subjected to vacuum measurement (n = 4), the temperature difference between the maximum and minimum increases again. This implies that the range of the MIT phase transformation can be tuned via tuning the oxygen vacancies.

Upon applying the same analysis in an in situ oxygen atmosphere measured sample, due to the continuous incorporation of the oxygen, no distinct single minimum or maximum could be seen, and instead, multiple peaks and valleys are seen. However, a similar trend to the vacuum measurement can be observed as shown in Figure 8b.

The transport in such correlated transition metal oxides happens via the polaron hopping mechanism. An attempt was made to understand the polaron hopping mechanism in the measured samples. The vacuum measurement provided an almost similar nature of the curve; therefore, only the third trial in vacuum measurement is included in the discussion for all the measured films where system is not undergoing any change when heated. As the LCO_25 film is measured rigorously in different conditions, the heating curve of the O_2-annealed film and the heating as well as cooling curve of the in situ measurement in O_2 are also analyzed. In the LCO films, the

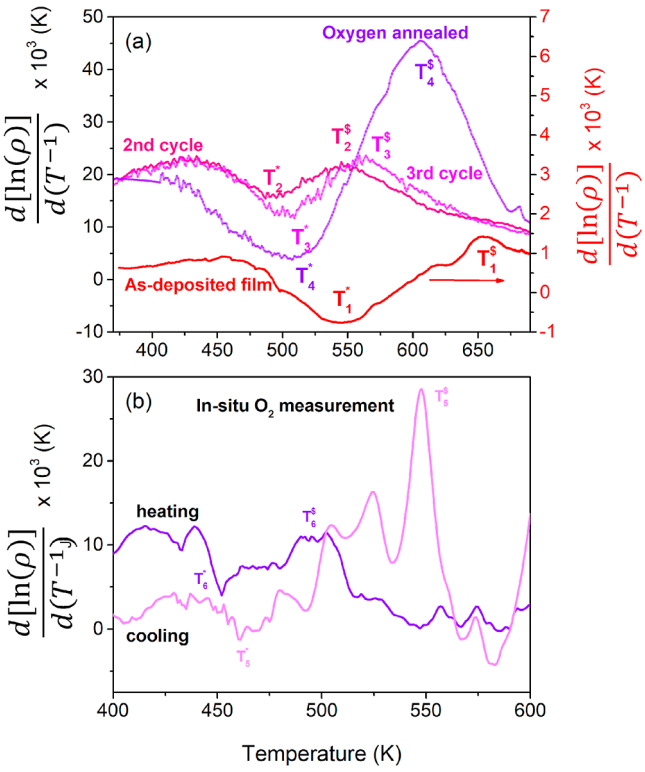

Figure 8. Temperature dependence of d $\ln(\rho)/d(T^{-1})$ for (a) as-prepared, vacuum-annealed, and oxygen-annealed samples and for (b) sample measured in an oxygen atmosphere.

heating curves consist of a hump in the mid temperature range (around 425−600 K). As previously mentioned, at the mid temperature range (100 K < T < 350 K), half of the Co^{3+} ions in the LS state undergo a spin state transition into Co^{3+} IS states. The transformation occurs gradually over the mentioned temperature range. This creates a huge disorder in this system and the material behaves as a Mott Insulator. In Mott insulators, at low temperature, the conduction happens through the variable range hopping (VRH) mechanism. Several reports support the VRH in the same and similar systems.[52,53] However, as the temperature further increases, the crossover in the conduction occurs. Continuous vacuum pumping helps create the deficiency of oxygen in the LCO and LSCO lattice sites, which as a result distorts the lattice. This distortion generates localized energy states for the carriers to be trapped, as mentioned by Emin.[54,55] The energy of these localized states is mainly modified by the electron−phonon small range interactions, which as a result consolidates the presence of small polarons in the high temperature range.[56,57] In the following section, the calculation of the interaction coupling constant also satisfies the presence of small polaron hopping (SPH). In between the small polaron formation and the VRH conduction, the crossover takes place over a certain temperature range (400−625 K).

The high temperature region before the crossover is well-fitted with the SPH model,[58] defined by

$$\frac{\rho(T)}{T} = \rho_\alpha \exp\left(\frac{E_a}{k_b T}\right) \tag{3}$$

where ρ_α is the pre-exponential factor, E_a is the polaron activation energy, and T is the absolute temperature. The activation energy, E_a, values were extracted near room

https://doi.org/10.1021/acsmaterialsau.3c00101
ACS Mater. Au 2024, 4, 308−323

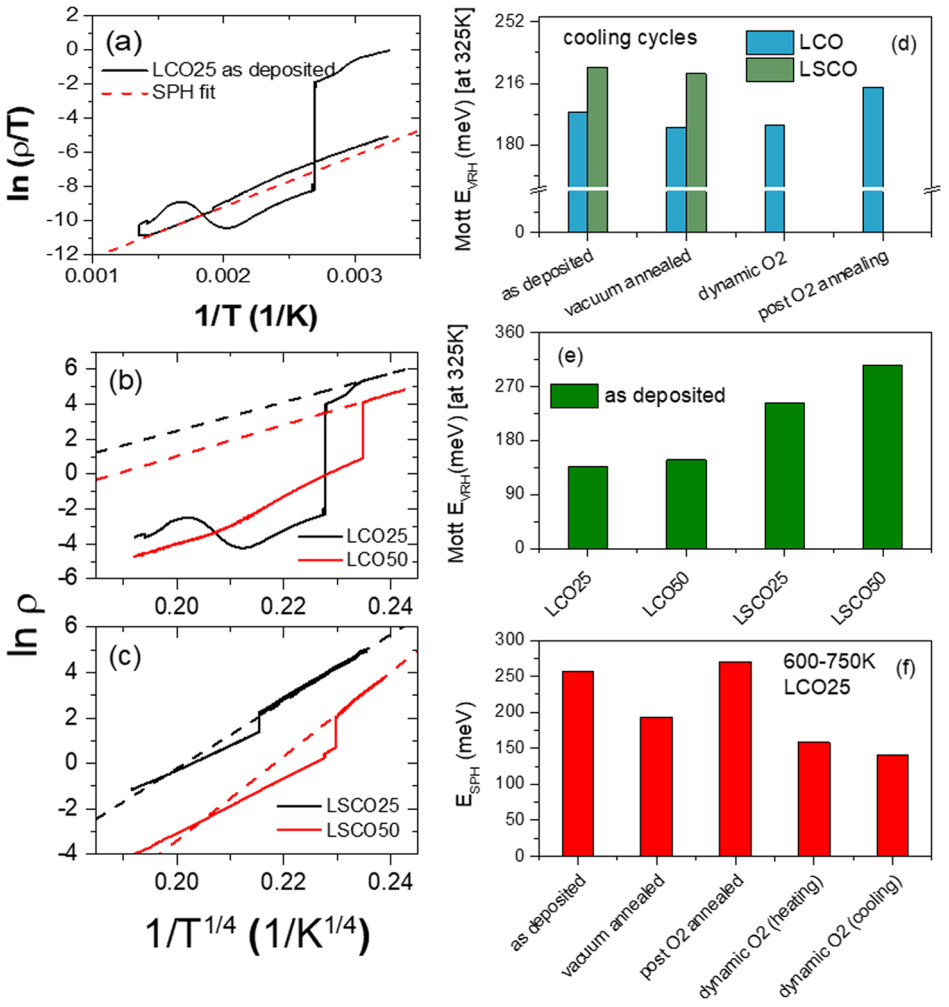

Figure 9. (a) SPH model fitting for the LCO_25 film for the 1st cooling cycle of resistivity at high temperature measured in vacuum. Mott VRH model fitting for the first heating cycle of the films (b) LCO_25 and LCO_50 and (c) LSCO_25 and LSCO_50 at low temperature before the step jump occurred in resistivity, measured in vacuum (d) Change in the $E_h/T^{3/4}$ (temperature independent) of the LCO_25 and LSCO_50 films under different measurement conditions. Comparison of (e) $E_h/T^{3/4}$ for the pristine films (as-deposited) of all samples and (f) E_{SPH} in the high temperature range (600−750 K) of the LCO_25 film in different measurement conditions.

temperature by the same formula $E_a = k_b\, d[\ln \rho]/d[1/T]$. This may be interpreted as at low temperatures, the hopping range increases and surpasses the distance between the nearest neighboring sites. The three-dimensional Mott's VRH mechanism is defined as

$$\rho(T) = \rho_0 \exp\left[\frac{T_0}{T}\right]^{1/4} \tag{4}$$

where ρ_0 is a constant and T_0 is the Mott's characteristic temperature. From this model, the hopping energy can be calculated by the formula shown in eq 5

$$E_h(T) = \frac{1}{4} k_b T \left[\frac{T_0}{T}\right]^{1/4} \tag{5}$$

The hopping energies with relevant temperature for the measurement curves are shown in Figure 9d,e which is in good agreement with the reported values.[52] Besides, representative figures of LCO_25 and LSCO_25 fitting for VRH are shown in Figure 9b,c.

A drastic change is observed as the hump appeared, depicting the two different hopping mechanisms with two different activation energies. The activation energies calculated are shown in Figure 9d−f. From the high temperature region, it is indicating the polaronic conduction between the nearest neighboring sites, and below 425 K the linearity of the curve shows deviation. Thus, the data may be divided into two regions, i.e., typically 600 K onward and in the range 300−425 K. In the first one (high temperature), it is found to obey SPH, whereas for the other (near room temperature) region, it is found to show Mott VRH. Figure 9a shows a typical SPH fit to LCO pristine sample data (cooling cycle), and Figure 9b,c shows three-dimensional Mott VRH fitting to as-deposited LCO and LSCO films, respectively. The data for VRH fitting and SPH fitting for the other trials are shown in Figures S7 and S8 in the Supporting Information.

The values of thermal activation energy are calculated in both the temperature ranges and are shown for comparison in Figure 9. In this VRH mechanism, it should be noted that the higher the activation energy, the nearer the hopping site. It is counterintuitive, but it may be explained as ref 59, where at low temperature, when the thermal energy is insufficient to rise to the nearer site with high energy, the carrier hops or tunnels to a farther site that if equivalent in energy. As temperature

https://doi.org/10.1021/acsmaterialsau.3c00101
ACS Mater. Au 2024, 4, 308−323

increases, the high energy site in proximity becomes accessible, and hence, the hopping distance reduces (eventually to the nearest neighbor limit and finally to band conduction). For large band gap systems, where these sites are deep within the band gap, the band conduction is difficult to establish and the conductivity is purely due to hopping.

3.4.1. Low Temperature (300−425 K) Range. In the low temperature range, in this case, the transport is dominated by the VRH mechanism. The energy is temperature-dependent (see eq 5). We found that LSCO has a consistently high energy ($E_{VRH}/T^{3/4}$ is temperature independent and hence can be compared across compositions). Besides, vacuum or oxygen annealing of LSCO does not lead to a significant variation in $E_{VRH}/T^{3/4}$. On the other hand, the value of the energy decreases upon vacuum annealing in LCO_25 and again increases when the sample is O_2-annealed (see Figure 9c). As mentioned above, it may be pointed out that the activation energy varies due to oxidation or reduction of Co^{3+} to Co^{4+} and vice versa due to the low or high oxygen content of the lattice prior to measurement. High lattice oxygen (in O_2 annealing) implies higher Co^{4+}, implying closer hopping sites and therefore high energy of activation. Similarly, low lattice oxygen (in vacuum annealing) implies lower Co^{4+}, implying farther hopping sites and therefore high energy of activation. On the other hand, in LSCO, the Co^{4+} fraction is less flexible due to the already present charge imbalance of Sr^{2+}. This pinning of the Co^{4+} fraction does not allow much scope for change in the range of hopping and hence no change in activation energy (see Figure 9d). The same also prevents LSCO to show complete conversion to a normal insulator, unlike LCO as discussed earlier.

3.4.2. High Temperature (600−750 K) Range. In the high temperature range, in this case, the transport is dominated by the SPH mechanism, where the hopping occurs via the nearest possible neighbor sites. The activation energy in this range is temperature independent and can be deduced from the slope of ln ρ vs $1/T$.[60] The values estimated for the LCO_25 film under different oxygen contents are shown in Figure 9f. To further consolidate the dominance of small polarons, it is evident to measure the temperature-dependent Seebeck coefficient to investigate the hopping energy manifested in thermopower. The thermopower S can be written as

$$S = \pm \frac{k_b}{e}\left(\frac{E_S}{k_b T} + B\right) \tag{6}$$

where E_S is the charge carrier generation energy and B is a constant. The small polaron activation energy E_a is a combination of mainly the polaron binding energies E_p and E_s (can be obtained from the temperature-dependent thermopower measurement) and related by eq 7[61,62]

$$E_a = \frac{E_p}{2} + E_s \tag{7}$$

However, due to the limitation of the experimental arrangements, it could not be measured. Moreover, the interaction coupling factor γ is calculated by the formulation described by Kim et al.[63] in eq 8.

$$\gamma = \frac{2E_a}{h\nu_0} \tag{8}$$

where h is the Planck's constant and ν_0 is the optical phonon frequency. The denominator in eq 6 is adopted from the reported value,[64] and the γ is found to be in the range of 4−10 for the different atmosphere processed LCO_25 films, as shown in Table S2 in the Supporting Information. As mentioned by Kim et al.[63] when the γ is greater than 4, strong electron−phonon interaction exists. It confirms the presence of small polarons.

As can be seen in Figure 9f, the activation energies of SPH for different atmosphere processed LCO films differ considerably. The hopping energies in the case of as-deposited and post-oxygen-annealed films are a bit higher. The rest are in a good agreement with the reported values of similar materials.[65,66] This probably appears because of the strong electron−phonon interaction in the distorted lattice of these films. The as-deposited film is amorphous; therefore, it should have a higher thermopower than its crystalline counterpart. However, the vacuum-annealed measurement assists the as-deposited films in improving their crystallinity, and the value of S decreases rapidly with the temperature increase and provides a higher charge carrier generation energy E_S for the polarons, as depicted in eq 6. Hence, the activation energy E_a becomes high. The vacuum-annealed film has already undergone crystallization and loss of lattice oxygen. A lower lattice oxygen content results in a low relative Co^{4+} fraction and hence low hopping energy, implying far apart hopping sites. As a dual effect of both crystallinity and hopping sites, a low activation energy is achieved. When annealed in oxygen, the Co^{4+} fraction increases and results in nearby hopping sites, and hence, the activation energy achieved the highest value. However, according to the in situ measurement, the activation energy decreased. Azulay et al. reported the anomaly in the activation energies with respect to the doping of La in $Ca_3Mn_2O_7$.[62] Similarly, the presence of different oxygen-deficient crystallites or the differential incorporation of O^- ions in different crystallites in in situ O_2 annealing may avert the films from exhibiting a systematic nature in the activation energy.[67] See Figure 10a for the relative Co^{2+}/Co^{3+} fraction.

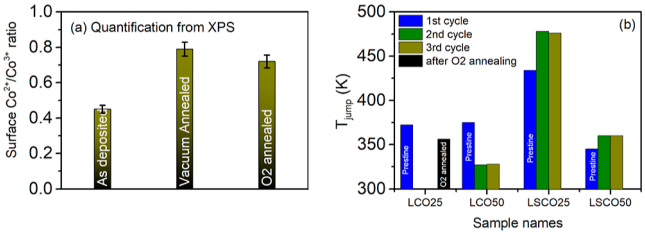

Figure 10. (a) Ratio of Co^{2+}/Co^{3+} ions probed by XPS at different stages of the sample during measurements. (b) Temperatures (T_{jump}) of different films at which the jump in resistivity occurred.

In the case of LSCO films, there is no crossover (MIT to normal insulator) observed in the experimental data. Therefore, it is possible that these LSCO films follow the same hopping mechanism throughout the entire temperature range. The whole experimental data are modeled with the VRH as well as before and the after the sudden jump in the temperature-dependent resistivity. Their jumps do not disappear even after the third vacuum annealing and are almost fixed in temperature. However, for LCO, the jump almost diminished in the first vacuum heating and reappeared after O_2 annealing (see Figure 10b)

https://doi.org/10.1021/acsmaterialsau.3c00101
ACS Mater. Au 2024, 4, 308−323

The surface chemical stoichiometry of Co charged states in different samples is shown in Figure 10a for all the three LCO samples.[68] In the as-deposited films, the surface ratio is found to be the least (about 45%). After the vacuum treatment, i.e., loss of oxygen, the ratio increased to about 80%, while in the oxygen-annealed film, expectedly, the ratio decreased from 80% to about 70%. As mentioned earlier, the presence of different oxidation in the Co ions can be substantiated by the appearance of the two satellite peaks. In the spectra presented in Figure 4d, for the as-deposited film, a small hump is observed around 789.7 eV. This corresponds to the octahedral Co^{3+} ions. A very feeble hump is seen at 786.8 eV, which may confirm the presence of tetrahedral Co^{2+} ions. The presence of this peak in the subsequent two measurements, i.e., vacuum-annealed as well as oxygen-annealed films, can be corroborated. Hence, it clearly states the improvement of the aforementioned ratio and confirms the distortion of the lattice.

Figure 10b shows the exact jump temperatures for each of the samples studied and after a given heat treatment. Comparing Figure 10a,b, it is clear that after vacuum annealing, there is an increase in the Co^{2+} fraction and the jump could not be seen. On the other hand, it reappears when the same vacuum-annealed film is oxygen-annealed, where the Co^{2+} fraction decreases slightly. Similarly, doping Sr leads to no crossover to a high δ value composition. Both, high thickness or Sr dopants, limit the oxygen intake window, depending on the thickness and Sr doping, and both do not allow a significant loss of oxygen, thereby restricting the transition to the high δ phase.

4. DISCUSSION

Most oxides spontaneously lose or gain oxygen depending on the partial pressure of oxygen in the ambient atmosphere and temperature of lattice, and the process is governed by diffusion. The extent of oxygen loss depends on the stability vis-à-vis affordability of each oxide.[69] Some lose in ppm at best, while some complex oxides lose in significant fractions. LCO and its doped derivatives belong to the latter class. The excessive loss of oxygen from the lattice sites (conversion toward $LaCoO_{2.5}$) leads to diminishing of the step jump feature and limits its application as a memory device. From the memory device perspective, the data are being stored in it like a rewritable compact disk. To replenish the storage system, the old data to be replaced with the new one, it requires a reset criterion. If the memory is made by using a material with the property of an amorphous (high resistance) to crystalline (low resistance) phase transition, an energized pulsed laser is used to destroy the crystallinity locally and make the film amorphous again to reset the disk. Extending this analogy to the present sample, the step jump feature was regained upon performing oxygen annealing as a reset button, just like the pulsed laser for rewriting a compact disk.

Among the grown films, the LCO_25 lost the step jump property in the first heating cycle itself. This film was annealed at 500 °C temperature in a 100% oxygen atmosphere, and measurements were performed on the oxygen-annealed film. The step jump was regained after oxygen annealing, as shown in Figure 7e. The reversible nature of step jump avalanches is thus confirmed for the lattice oxygen content. To further confirm the effect of oxygen in this restoration phenomenon, the sample was measured in a dynamic oxygen atmosphere, as discussed previously, and it is shown in Figure 7d. Surprisingly, it resulted with a multistage resistivity jump during cooling.

In the present work, the step-like resistive avalanches are the significant findings seen for first time in LCO to the best of our knowledge. Unlike VO_2, the MIT in this system is not known to show such a drastic first order change. For the as-deposited LCO films, in the heating cycle, the sudden jump was found to be at 372 K, and for the cooling cycle, it did not show any transition until room temperature (300 K). However, in the case of LSCO films, the thermal hysteresis was found to be minimal, and the sudden jump was detected at 434 K during heating and, like LCO, not found during cooling. However, for a little thicker film whose data are presented in the Supporting Information, the pristine films of LCO_50 show the sudden jumps at 376 and 334 K for heating and cooling, respectively. Similarly, the pristine films of LSCO show the sudden jumps at 345 and 354 K for heating and cooling, respectively. On subsequent heating, the hysteresis between heating and cooling is substantially reduced, and particularly for the LSCO film, it occurs almost at the same temperature.

In the single crystal or polycrystalline LCO (or LSCO), bulk samples show a prominent gradual metal insulator transition, albeit no sudden jumps are observed at any temperature. Nonetheless, in the case of sputtered thin films, the nucleation takes place through formation of islands of the material called nuclei, followed by crystallization and growth. LCO or LSCO thin films are often grown on the epitaxial substrates like $LaAlO_3$ or $SrTiO_3$ that have similar lattice structures with minimal lattice mismatch. The growth of LCO films on these substrates leads to epitaxy with a high crystalline orientation. A strain may get induced[70] due to the small but finite lattice mismatch. The Si/SiO_2 substrate due to its amorphous nature may not lead to any epitaxy or be expected to produce any strain. Besides, the room temperature deposition does not provide the required energy for crystallization. Thus, the as-prepared films are amorphous, as seen in the XRD patterns (Figure 2). Therefore, the films are free of any lattice strain. Upon first heating in vacuum, the crystallization coupled with oxygen stoichiometry evolution results in a unique step-like change in resistivity. Instead of a continuous, oriented film, this process of thin film growth leads to polycrystalline small domains of materials all over the uniform thickness films. This is substantiated by the two different (110) and (104) peaks in XRD reflections from the film, which are otherwise dominant in polycrystalline XRD too. As a result, the films are polycrystalline with a distribution of size in individual crystallites. Besides, as discussed in the preceding sections, the crystal anisotropy may be significant to induced direction dependence in electrical conductivity as it arises from hopping of carriers. Thus, there may be a gradual change in conductivity of different crystallites depending on the crystalline orientation with respect to the applied field and size. Hence, the transformation (from the insulator to metal phase) time may vary from crystallite to crystallite depending on the size as well as crystal orientation. Thus, dynamically, the metallic phase evolves over the process among these crystallites continuously. As soon as the percolation is established among the metallic channels, a sudden step fall may result in the resistance. Besides, owing to the thickness of the film (125 nm), it may be possible that the percolation is predominantly two-dimensional in nature unlike bulk three-dimensional solid where multiple parallel channels from bulk keep establishing and resulting in gradual drop in resistivity.

In addition to the size and orientation of the crystallites, the oxygen content of the crystallites has a decisive role in this

https://doi.org/10.1021/acsmaterialsau.3c00101
ACS Mater. Au 2024, 4, 308−323

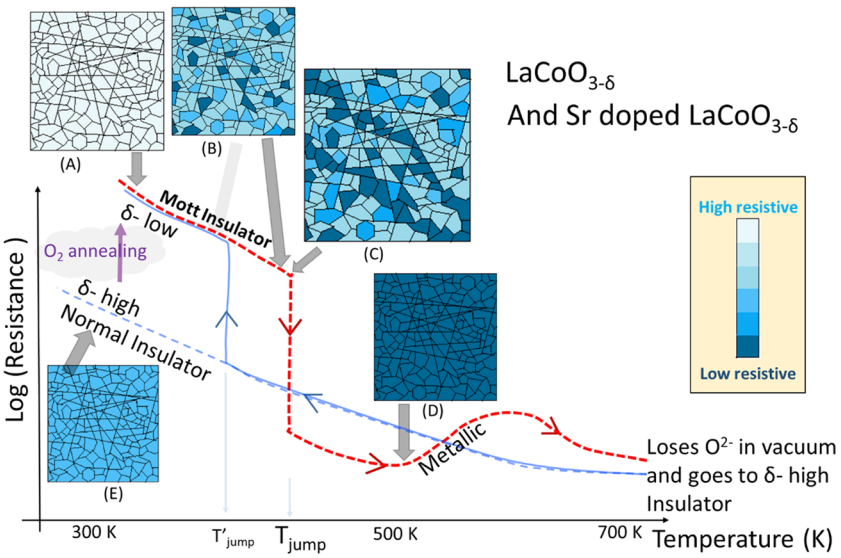

Figure 11. Schematic diagram to explain the sudden jump (avalanches) in the resistance Vs temperature measurement of LCO films. (A) As-deposited amorphous LCO film, (B) vacuum-heated LCO film with the dynamic loss of O_2, (C) critical loss of O_2 due to heating and resulting in a percolative conduction path, and (D) metallic phase with complete conversion later to another insulating phase due to the excessive loss of oxygen (high δ). Upon cooling, the crystallite goes back to the high resistance state, leading to the breaking of the percolation. (E) The high resistance state may evolve two ways, either it remains in the high δ (BM phase) with a normal insulator-like behavior or the thickness and/or Sr doping prevents excessive O_2 loss and the Mott insulator property—perovskite structure is restored.

process, as observed in our results. It may be explained with the help of Figure 11, as follows. Crystallites with the highest resistance are represented by the lightest shade. The color depth renders the resistance of the film, as shown in the color scale bar in Figure 11. The first image (Figure 11A) represents the as-deposited film consisting of a broad distribution in size of the crystallites with the overall highest resistance state. As it is heated, the film crystallizes and the change in resistance of each of the crystallites shall differ with the change in the size, crystal orientation, and possible degree of variance in the oxygen content in each crystallite (the δ value may not be precisely the same for all the crystallites). Let T_{jump} represent the temperature at which the jump appears in the ρ vs T plots. For $T < T_{jump}$ in the first cycle of the measurement in vacuum, few of these crystallites undergo phase transition to the low resistive state compared to the rest, as shown in the second film (B) by the lower number of darker crystallites. When the temperature is increased further similarly, the other crystallites start conducting more. Suddenly, at $T = T_{jump}$, high conducting crystallites form a percolation path with the increase in temperature, and the jump occurs in the resistance, as shown in the third film (C) image of the figure. This further converts completely to the metallic phase (D) and start to exhibit a positive slope in the R vs T curve. At significantly high temperature, the film surface loses a substantial amount of the oxygen and may have Co^{2+} presence to go to another insulating (BM like) phase.

During the cooling process, the crystallites cool down in a similar fashion. This disconnects the percolation paths present as they become high resistance. At a critical temperature, all the percolation paths break and the system may go back to the Mott insulator phase with a delta value similar to or slightly higher than that of the initial film, as shown in the film image. After several trials in vacuum, the total film settles down to a relatively low resistivity (high δ) film than the as-deposited one at room temperature, as shown in the Figure 11E film image. When the same film is further annealed in oxygen, it enhances the resistance of the film. However, the resistance value does not restore the value of the virgin film, as shown in the sixth film image in Figure 11.

On the other hand, in the LSCO films (doping Sr in LCO), the step jump is observed too; however, in the first trial of measurement (after crystallization) and the further trials, the step jumps are retained at almost the same temperature during heating as well as cooling for the individual LSCO film. So, for the LSCO films, the heating and oxygen extraction affected the formation of the films differently. As pointed out earlier, in LSCO, after the first heating, the oxygen loss is low due to the Sr doping (or high thickness materials). Hence, only the Mott insulator to metal transition of most of the crystallites created the percolation path and gave a step jump at a fixed temperature for an individual film, as is observed in VO_2 films reported by Genchi et al.[15]

5. CONCLUSIONS

To summarize, the LCO and LSCO thin films were grown on a Si/SiO_2 substrate by the RF sputtering process. The structural and the electrical transport properties of the polycrystalline LCO and LSCO thin films were investigated with different heat treatments. The as-deposited films were amorphous in nature, as seen in the XRD patterns. Continuous $R-T$ measurement in vacuum for the LCO films exhibited a sharp MIT in resistance followed by crystallization to a normal insulator phase as seen during cooling. This is ascribed to the loss of oxygen from the films, leading to the rise of Co^{2+} ions. The conduction process is dominated by the double exchange mechanism. At a certain temperature, a percolation path is established among the crystallites of the film, which gave rise to the sudden jump in the resistance when the first percolation path emerges. The loss of oxygen induced phase transition of the crystal structure toward its oxygen-deficient (normal insulating) phase, diminished the jump in resistance and seldom a confined range of temperature MIT was observed. With the several heating—cooling cycles in vacuum, the

https://doi.org/10.1021/acsmaterialsau.3c00101
ACS Mater. Au 2024, 4, 308−323

confined range decreased and the LCO films lost their step jump characteristics. By annealing in oxygen, the said characteristic was partially regained. The uninterrupted measurement in the oxygen atmosphere displayed the unique characteristics of the multistage step jump in resistance due to the continuous incorporation of oxygen in the films. From the XPS data, the rise of Co^{2+} or even Co^{4+} oxidation states supported the described mechanism of a normal insulator and a Mott insulator, respectively. Further, for the LSCO films, a transition from insulator 1 to insulator 2 was spotted as the step jump occurred. Unlike LCO, with the subsequent measurements in vacuum, the jump in resistance was retained at a particular temperature for the LSCO film. The transport is modeled using the Mott formula and SPH model. It is observed that the vacuum annealing of LCO shows a crossover from the Mott insulator to normal insulator with an SPH type of conduction. However, oxygen-annealed LCO and LSCO (both contain Co^{4+}) show a Mott type VRH mechanism. The concentration of Co^{4+} predominantly governs their relative distance and hence also governs the energy of hopping.

■ ASSOCIATED CONTENT

Data Availability Statement

The data are available from the corresponding author with a reasonable request.

Supporting Information

The Supporting Information is available free of charge at https://pubs.acs.org/doi/10.1021/acsmaterialsau.3c00101.

The crystal structure of perovskite $LaCoO_3$ and BM $LaCoO_{2.5}$, thin film deposition parameters and film thickness, XRD patterns of LCO50 and LSCO50, device $I-V$ characteristics and bare Si substrate data, and SPH and VRH model fitting (PDF)

■ AUTHOR INFORMATION

Corresponding Author

Vinayak B. Kamble − *School of Physics, Indian Institute of Science Education and Research, Thiruvananthapuram 695551, India;* orcid.org/0000-0002-6344-2194; Email: kbvinayak@iisertvm.ac.in

Authors

Soumya Biswas − *School of Physics, Indian Institute of Science Education and Research, Thiruvananthapuram 695551, India*

Noora Naushad − *School of Physics, Indian Institute of Science Education and Research, Thiruvananthapuram 695551, India*

Kalyani S − *School of Physics, Indian Institute of Science Education and Research, Thiruvananthapuram 695551, India*

Complete contact information is available at: https://pubs.acs.org/10.1021/acsmaterialsau.3c00101

Author Contributions

V.K. and S.B. conceived of the presented idea. V.K. and S.B. planned the experiments, and S.B., N.N., and S.K. carried out the experiments. V.K. encouraged S.B. to investigate the oxygen doping effects and supervised the findings of this work. S.B. wrote the first draft, and all authors contributed to the final version of the manuscript. All authors discussed the results and contributed to the final manuscript. CRediT: **SOUMYA BISWAS** conceptualization, data curation, formal analysis, investigation, methodology, validation, writing-original draft, writing-review & editing; **Noora Naushad** data curation, investigation; **Kalyani S** data curation, investigation; **Vinayak B Kamble** formal analysis, funding acquisition, investigation, project administration, resources, supervision, validation, writing-review & editing.

Notes

The authors declare no competing financial interest.

■ REFERENCES

(1) Casanova, F.; Labarta, A.; Batlle, X.; Pérez-Reche, F. J.; Vives, E.; Mañosa, L.; Planes, A. Direct observation of the magnetic-field-induced entropy change in $Gd_5(Si_xGe_{1-x})_4$ giant magnetocaloric alloys. *Appl. Phys. Lett.* **2005**, *86*, 262504.

(2) Cote, P. J.; Meisel, L. V. Self-organized criticality and the Barkhausen effect. *Phys. Rev. Lett.* **1991**, *67*, 1334−1337.

(3) Puppin, E. Statistical Properties of Barkhausen Noise in Thin Fe Films. *Phys. Rev. Lett.* **2000**, *84*, 5415−5418.

(4) Pérez-Reche, F. J.; Tadić, B.; Mañosa, L.; Planes, A.; Vives, E. Driving Rate Effects in Avalanche-Mediated First-Order Phase Transitions. *Phys. Rev. Lett.* **2004**, *93*, 195701.

(5) Carrillo, L.; Mañosa, L.; Ortín, J.; Planes, A.; Vives, E. Experimental Evidence for Universality of Acoustic Emission Avalanche Distributions during Structural Transitions. *Phys. Rev. Lett.* **1998**, *81*, 1889−1892.

(6) Chattopadhyay, T.; Pannetier, J.; Von Schnering, H. G. Neutron diffraction study of the structural phase transition in SnS and SnSe. *J. Phys. Chem. Solids* **1986**, *47*, 879−885.

(7) Łażewski, J.; Sternik, M.; Jochym, P. T.; Kalt, J.; Stankov, S.; Chumakov, A. I.; Göttlicher, J.; Rüffer, R.; Baumbach, T.; Piekarz, P. Lattice Dynamics and Structural Phase Transitions in Eu_2O_3. *Inorg. Chem.* **2021**, *60*, 9571−9579.

(8) Janod, E.; Tranchant, J.; Corraze, B.; Querré, M.; Stoliar, P.; Rozenberg, M.; Cren, T.; Roditchev, D.; Phuoc, V. T.; Besland, M.-P.; Cario, L. Resistive Switching in Mott Insulators and Correlated Systems. *Adv. Funct. Mater.* **2015**, *25*, 6287−6305.

(9) Zou, T.; Peng, J.; Gottschalk, M.; Zhang, P. P.; Mao, Z. Q.; Ke, X. Insulator−metal transition induced by electric voltage in a ruthenate Mott insulator. *J. Phys.: Condens. Matter* **2019**, *31*, 195602.

(10) Kalcheim, Y.; Camjayi, A.; del Valle, J.; Salev, P.; Rozenberg, M.; Schuller, I. K. Non-thermal resistive switching in Mott insulator nanowires. *Nat. Commun.* **2020**, *11*, 2985.

(11) Pirovano, A.; Lacaita, A. L.; Benvenuti, A.; Pellizzer, F.; Bez, R. Electronic switching in phase-change memories. *IEEE Trans. Electron Devices* **2004**, *51*, 452−459.

(12) Ozatay, O.; Stipe, B.; Katine, J. A.; Terris, B. D. Electrical switching dynamics in circular and rectangular $Ge_2Sb_2Te_5$ nanopillar phase change memory devices. *J. Appl. Phys.* **2008**, *104*, 084507.

(13) Cheng, H.-Y.; Raoux, S.; Chen, Y.-C. The impact of film thickness and melt-quenched phase on the phase transition characteristics of $Ge_2Sb_2Te_5$. *J. Appl. Phys.* **2010**, *107*, 074308.

(14) Brito, W. H.; Aguiar, M. C. O.; Haule, K.; Kotliar, G. Metal-Insulator Transition in VO2: A DFT\DMFT Perspective. *Phys. Rev. Lett.* **2016**, *117*, 056402.

(15) Genchi, S.; Yamamoto, M.; Iwasaki, T.; Nakaharai, S.; Watanabe, K.; Taniguchi, T.; Wakayama, Y.; Tanaka, H. Step-like resistance changes in VO_2 thin films grown on hexagonal boron nitride with in situ optically observable metallic domains. *Appl. Phys. Lett.* **2022**, *120*, 053104.

(16) Sharoni, A.; Ramírez, J. G.; Schuller, I. K. Multiple Avalanches across the Metal-Insulator Transition of Vanadium Oxide Nanoscaled Junctions. *Phys. Rev. Lett.* **2008**, *101*, 026404.

(17) Durand, A. M.; Belanger, D. P.; Booth, C. H.; Ye, F.; Chi, S.; Fernandez-Baca, J. A.; Bhat, M. Magnetism and phase transitions in $LaCoO_3$. *J. Phys.: Condens. Matter* **2013**, *25*, 382203.

(18) Posadas, A.; Berg, M.; Seo, H.; Smith, D. J.; Kirk, A. P.; Zhernokletov, D.; Wallace, R. M.; de Lozanne, A.; Demkov, A. A. Strain-induced ferromagnetism in $LaCoO_3$: Theory and growth on Si (100). *Microelectron. Eng.* **2011**, *88*, 1444−1447.
(19) Yoon, S.; Gao, X.; Ok, J. M.; Liao, Z.; Han, M.-G.; Zhu, Y.; Ganesh, P.; Chisholm, M. F.; Choi, W. S.; Lee, H. N. Strain-Induced Atomic-Scale Building Blocks for Ferromagnetism in Epitaxial $LaCoO_3$. *Nano Lett.* **2021**, *21*, 4006−4012.
(20) Meng, D.; Guo, H.; Cui, Z.; Ma, C.; Zhao, J.; Lu, J.; Xu, H.; Wang, Z.; Hu, X.; Fu, Z.; Peng, R.; Guo, J.; Zhai, X.; Brown, G. J.; Knize, R.; Lu, Y. Strain-induced high-temperature perovskite ferromagnetic insulator. *Proc. Natl. Acad. Sci. U.S.A.* **2018**, *115*, 2873−2877.
(21) Fuchs, D.; Merz, M.; Nagel, P.; Schneider, R.; Schuppler, S.; von Löhneysen, H. Double Exchange via t_{2g} Orbitals and the Jahn-Teller Effect in Ferromagnetic $La_{0.7}Sr_{0.3}CoO_3$ Probed by Epitaxial Strain. *Phys. Rev. Lett.* **2013**, *111*, 257203.
(22) An, Q.; Xu, Z.; Wang, Z.; Meng, M.; Guan, M.; Meng, S.; Zhu, X.; Guo, H.; Yang, F.; Guo, J. Tuning of the oxygen vacancies in $LaCoO_3$ films at the atomic scale. *Appl. Phys. Lett.* **2021**, *118*, 081602.
(23) Noskin, L. E. Study of the metal-insulator transition in $LaCoO_{3-x}$ epitaxial films. M.Sc. Thesis, Cornell University, 2018; Vol. 3, pp 1−12.
(24) Li, X.-j.; Wang, B.-T.; Yin, W. Octahedral rotation induced spin state and metal−insulator transition in $LaCoO_3$ films. *J. Magn. Magn. Mater.* **2022**, *555*, 169318.
(25) Tokura, Y.; Okimoto, Y.; Yamaguchi, S.; Taniguchi, H.; Kimura, T.; Takagi, H. Thermally induced insulator-metal transition in LaCoO3: A view based on the Mott transition. *Phys. Rev. B* **1998**, *58*, R1699−R1702.
(26) Okimoto, Y.; S, T.; Kobayashi, Y.; Ishihara, S. *Spin-Crossover Cobaltite*; Springer Singapore, 2021; Vol. *10*, pp 978−981.
(27) Kharkhan, D. N.; Pilloud, D.; Bruyère, S.; Migot, S.; Barrat, S.; Capon, F. Influence of as-deposited non-uniform stoichiometry on thermochromic properties of $LaCoO_3$ selective layers. *J. Appl. Phys.* **2020**, *127*, 015304.
(28) Celorrio, V.; Dann, E.; Calvillo, L.; Morgan, D. J.; Hall, S. R.; Fermin, D. J. Oxygen Reduction at Carbon-Supported Lanthanides: The Role of the B-Site. *ChemElectroChem* **2016**, *3*, 283−291.
(29) Sadabadi, H.; Allahkaram, S. R.; Kordijazi, A.; Akbarzadeh, O.; Rohatgi, P. K. Structural characterization of $LaCoO_3$ perovskite nanoparticles synthesized by sol−gel autocombustion method. *Eng. Rep.* **2021**, *3*, No. e12335.
(30) Cullity, B. D. *Elements of X-Ray Diffraction*; Addison-Wesley Publishing Company, 1956.
(31) Holder, C. F.; Schaak, R. E. Tutorial on Powder X-ray Diffraction for Characterizing Nanoscale Materials. *ACS Nano* **2019**, *13*, 7359−7365.
(32) Ohring, M. Chapter 10 - Characterization of Thin Films and Surfaces. In *Materials Science of Thin Films* 2nd ed., Ohring, M., Ed. Academic Press: San Diego, 2002; pp 559−640.
(33) Ying, Y.; Fan, J.; Pi, L.; Qu, Z.; Wang, W.; Hong, B.; Tan, S.; Zhang, Y. Effect of Ru doping in $La_{0.5}Sr_{0.5}MnO_3$ and $La_{0.45}Sr_{0.55}MnO_3$. *Phys. Rev. B* **2006**, *74*, 144433.
(34) Zhang, Q.; Gao, A.; Meng, F.; Jin, Q.; Lin, S.; Wang, X.; Xiao, D.; Wang, C.; Jin, K.-j.; Su, D.; Guo, E.-J.; Gu, L. Near-room temperature ferromagnetic insulating state in highly distorted $LaCoO_{2.5}$ with CoO_5 square pyramids. *Nat. Commun.* **2021**, *12*, 1853.
(35) Granados, X.; Fontcuberta, J.; Obradors, X.; Torrance, J. B. Metastable metallic state and hysteresis below the metal-insulator transition in $PrNiO_3$. *Phys. Rev. B* **1992**, *46*, 15683−15688.
(36) Grygiel, C.; Pautrat, A.; Prellier, W.; Mercey, B. Hysteresis in the electronic transport of V_2O_3 thin films: Non-exponential kinetics and range scale of phase coexistence. *Europhys. Lett.* **2008**, *84*, 47003.
(37) Ichimura, K.; Inoue, Y.; Yasumori, I. Catalysis by Mixed Oxide Perovskites. I. Hydrogenolysis of Ethylene and Ethane on $LaCoO_3$. *Bull. Chem. Soc. Jpn.* **1980**, *53*, 3044−3049.
(38) Ichimura, K.; Inoue, Y.; Yasumori, I. Catalysis by Mixed Oxide Perovskites. II. The Hydrogenolysis of C3−C5 Hydrocarbons on $LaCoO_3$. *Bull. Chem. Soc. Jpn.* **1981**, *54*, 1787−1792.
(39) Wang, X.; Peng, X.; Ran, H.; Lin, B.; Ni, J.; Lin, J.; Jiang, L. Influence of Ru Substitution on the Properties of $LaCoO_3$ Catalysts for Ammonia Synthesis: XAFS and XPS Studies. *Ind. Eng. Chem. Res.* **2018**, *57*, 17375−17383.
(40) Behera, S.; Kamble, V.; Vitta, S.; Umarji, A.; Shivakumara, C. Synthesis, structure and thermoelectric properties of $La_{1-x}Na_xCoO_3$ perovskite oxides. *Bull. Mater. Sci.* **2017**, *40*, 1291−1299.
(41) Biesinger, M. C.; Payne, B. P.; Grosvenor, A. P.; Lau, L. W. M.; Gerson, A. R.; Smart, R. S. C. Resolving surface chemical states in XPS analysis of first row transition metals, oxides and hydroxides: Cr, Mn, Fe, Co and Ni. *Appl. Surf. Sci.* **2011**, *257*, 2717−2730.
(42) Zhang, S.; Galli, G. Understanding the metal-to-insulator transition in $La_{1-x}Sr_xCoO_{3-\delta}$ and its applications for neuromorphic computing. *npj Comput. Mater.* **2020**, *6*, 170.
(43) Okazaki, R.; Tomiyasu, K. Prominent electron-hole asymmetry in thermoelectric transport of LaCoO3. *Phys. Rev. B* **2022**, *105*, 035154.
(44) Kumar, A.; Sivaprahasam, D.; Thakur, A. D. Improved thermoelectric properties in (1-x)LaCoO3/(x)La0.7Sr0.3CoO3 composite. *Mater. Chem. Phys.* **2021**, *269*, 124750.
(45) Kumar, A.; Dragoe, D.; Berardan, D.; Dragoe, N. Thermoelectric properties of high-entropy rare-earth cobaltates. *J Mater.* **2023**, *9*, 191−196.
(46) Kumar, A.; Sivaprahsam, D.; Thakur, A. D. Improvement of thermoelectric properties of lanthanum cobaltate by Sr and Mn co-substitution. *J. Alloys Compd.* **2018**, *735*, 1787−1791.
(47) Berggold, K.; Kriener, M.; Zobel, C.; Reichl, A.; Reuther, M.; Müller, R.; Freimuth, A.; Lorenz, T. Thermal conductivity, thermopower, and figure of merit of La1-xSrxCoO3. *Phys. Rev. B* **2005**, *72*, 155116.
(48) Kriener, M.; Zobel, C.; Reichl, A.; Baier, J.; Cwik, M.; Berggold, K.; Kierspel, H.; Zabara, O.; Freimuth, A.; Lorenz, T. Structure, magnetization, and resistivity of La1-xMxCoO3, M = Sr, Ba. *Phys. Rev. B* **2004**, *69*, 094417.
(49) Yamaguchi, S.; Okimoto, Y.; Taniguchi, H.; Tokura, Y. Spin-state transition and high-spin polarons in $LaCoO_3$. *Phys. Rev. B* **1996**, *53*, R2926−R2929.
(50) Yamaguchi, S.; Okimoto, Y.; Tokura, Y. Bandwidth dependence of insulator-metal transitions in perovskite cobalt oxides. *Phys. Rev. B* **1996**, *54*, R11022−R11025.
(51) Alagoz, H. S.; Živković, I.; Chow, K. H.; Jung, J. Non-percolating small metallic clusters and sharp suppression of metallicity in $RE_{0.55}Sr_{0.45}Mn_{1-x}Ru_xO_3$ manganites. *Phys. Chem. Chem. Phys.* **2018**, *20*, 2431−2437.
(52) Kumar, A.; Kumar, R.; Kumar, V.; Shukla, D.; Choudhary, R. J.; Kumar, R. 200 MeV Ag+15 ion irradiation-induced modification in structural, magnetic and electrical properties of $LaCoO_3$ thin film. *Appl. Phys. A: Mater. Sci. Process.* **2020**, *126*, 499.
(53) Liu, B.; Wang, Y.; Liu, G.; Feng, H.; Yang, H.; Sun, J. Electrical transport properties of $La_{1-x}Sr_xCoO_3$ thin films. *J. Appl. Phys.* **2016**, *120*, 154103.
(54) Strong coupling: self-trapping. In *Polarons*; Emin, D., Ed.; Cambridge University Press: Cambridge, 2012; pp 21−42.
(55) Franchini, C.; Reticcioli, M.; Setvin, M.; Diebold, U. Polarons in materials. *Nat. Rev. Mater.* **2021**, *6*, 560−586.
(56) Kabir, R.; Zhang, T.; Wang, D.; Donelson, R.; Tian, R.; Tan, T. T.; Li, S. Improvement in the thermoelectric properties of $CaMnO_3$ perovskites by W doping. *J. Mater. Sci.* **2014**, *49*, 7522−7528.
(57) Azulay, A.; Wahabi, M.; Natanzon, Y.; Kauffmann, Y.; Amouyal, Y. Enhanced Charge Transport in Ca2MnO4-Layered Perovskites by Point Defect Engineering. *ACS Appl. Mater. Interfaces* **2020**, *12*, 49768−49776.
(58) Rudra, M.; Halder, S.; Saha, S.; Dutta, A.; Sinha, T. P. Temperature dependent conductivity mechanisms observed in Pr_2NiTiO_6. *Mater. Chem. Phys.* **2019**, *230*, 277−286.

https://doi.org/10.1021/acsmaterialsau.3c00101
ACS Mater. Au 2024, 4, 308−323

(59) Lösche, A. *Electronic Processes in Non-crystalline Materials Clarendon-Press*; John Wiley & Sons, Ltd: Oxford, 1972; Vol. *7*, pp K55−K56.
(60) Vijay, A.; S, C. P.; Jose, R.; Saravanan K, V. Enhancement in the electrical transport properties of $CaMnO_3$ via La/Dy co-doping for improved thermoelectric performance. *RSC Adv.* **2023**, *13*, 19651−19660.
(61) Gayner, C.; Natanzon, Y.; Amouyal, Y. Effects of Co-doping and Microstructure on Charge Carrier Energy Filtering in Thermoelectric Titanium-Doped Zinc Aluminum Oxide. *ACS Appl. Mater. Interfaces* **2022**, *14*, 4035−4050.
(62) Azulay, A.; Leibovitz, T.; Natanzon, Y.; Zabari, O.; Amouyal, Y. $Ca_3Mn_2O_7$-layered perovskites: Effects of La- and Y-doping on phase stability, microstructure, and thermoelectric transport. *J. Am. Ceram. Soc.* **2023**, *106*, 213−226.
(63) Kim, M.; Mori, S.; Shuang, Y.; Hatayama, S.; Ando, D.; Sutou, Y. Electrical Conduction Mechanism of β-MnTe Thin Film with Wurtzite-Type Structure Using Radiofrequency Magnetron Sputtering. *Phys. Status Solidi RRL* **2022**, *16*, 2100641.
(64) Golosova, N. O.; Kozlenko, D. P.; Kolesnikov, A. I.; Kazimirov, V. Y.; Smirnov, M. B.; Jirák, Z.; Savenko, B. N. Evolution of the phonon density of states of $LaCoO_3$ over the spin state transition. *Phys. Rev. B* **2011**, *83*, 214305.
(65) Aswin, V.; Kumar, P.; Singh, P.; Gupta, A.; Rayaprol, S.; Dogra, A. Influence of Al doping in $LaCoO_3$ on structural, electrical and magnetic properties. *J. Mater. Sci.* **2015**, *50*, 366−373.
(66) U, D. S.; Rao, A.; Mukherjee, B.; Okram, G. S.; Davis, N.; Ashok, A. M.; Poornesh, P. Incorporation of copper in $LaCoO_3$: modulating thermoelectric power factor for low- and mid-temperature thermoelectric applications. *J. Mater. Sci.: Mater. Electron.* **2023**, *34*, 1893.
(67) Azulay, A.; Wahabi, M.; Natanzon, Y.; Kauffmann, Y.; Amouyal, Y. Correlation between charge transport and lattice dynamics in La- and Y-doped Ca_2MnO_4 perovskites. *Acta Mater.* **2023**, *259*, 119293.
(68) Thornton, G.; Orchard, A. F.; Rao, C. N. R. A study of $LaCoO_3$ and related materials by X-ray photoelectron spectroscopy. *J. Phys. C: Solid State Phys.* **1976**, *9*, 1991−1998.
(69) Gunkel, F.; Christensen, D. V.; Chen, Y. Z.; Pryds, N. Oxygen vacancies: The (in)visible friend of oxide electronics. *Appl. Phys. Lett.* **2020**, *116*, 120505.
(70) Li, Y.; Peng, S. J.; Wang, D. J.; Wu, K. M.; Wang, S. H. Strain effect on the magnetic and transport properties of $LaCoO_3$ thin films. *AIP Adv.* **2018**, *8*, 056317.

https://doi.org/10.1021/acsmaterialsau.3c00101
ACS Mater. Au 2024, 4, 308−323